Dissociation dynamics of highly excited molecules: Theory and Experiment

Oghbaie, Shabnam

2017

Dissociation dynamics of highly excited molecules: Theory and Experiment

Doctoral thesis

by

Shabnam Oghbaie

Division of Synchrotron Radiation Research
Department of Physics
Lund University

Division of Synchrotron Radiation Research
Department of Physics
Lund University
BOX 118
SE-221 00 LUND, SWEDEN
ISBN 978-91-7753-262-0 (print)
ISBN 978-91-7753-263-7 (pdf)

Printed in Lund, Sweden, April 2017, by Mediatryck

Abstract

This thesis presents studies on dissociation of two model molecules: Butadiene and Cyclopropane. Tunable synchrotron radiation was used to ionize or excite the molecules in the gas phase, and the momentum correlation of the resulting fragment ions were measured using a 3D momenta coincident ion spectroscopy. The experimental results were interpreted with the aid of *ab-initio* quantum calculation. This allows us to gain insight into the fundamental processes behind the molecular dissociation, that how correlated electronic and nuclear dynamics drive molecular dissociation.

Tunable XUV-radiation was used to doubly ionize molecules to different states. By Comparing experimental and theoretical values for appearance energy and kinetic energy released of the dissociation channels, electronic gateway state of each dissociation channels were identified. By analysing the momentum vector of ion pairs as a function of photon energy and internal energy sharing in the dissociative double ionization channels, mechanisms of double ionization (direct or indirect) processes were investigated. The studies shed light on the electron-electron and electron-nuclear correlation effects in the molecules.

Tunable X-rays were used to selectively excite a localized core electron to different valence orbitals, and the subsequent autoionization and dissociation processes were studied by analysing the correlated momentum of ionic fragments. In butadiene, the dependence of molecular dissociation on the initial site of core-hole was studied for the chemically shifted terminal and central carbon core-electrons excitation. In cyclopropane the dependence of molecular dissociation on the changing of the molecular bonding character was studied for different core-to-valence excitations. The studies indicated the importance of the ultra-fast nuclear dynamics initiated within a few femtosecond core-hole lifetime changing the picture of electron-electron correlation in autoionization processes and leading to specific dissociation channels.

Preface

This thesis reports theoretical and experimental studies on the fragmentation of free molecules. The body of this work is consisted of the following papers, which in the text are referred to as paper I, paper II, paper III, paper IV, and paper V.

I. Dissociative double-photoionization of butadiene in the 25-45 eV energy range using 3-D multi-coincidence ion momentum imaging spectrometry

Shabnam Oghbaie, Mathieu Gisselbrecht, Joakim Laksman, Erik. P. Månsson, Anna Sankari, and Stacey. L. Sörensen
J. Chem. Phys. **143**, 114309 (2015)

Tunable XUV-radiation was used to doubly ionize butadiene. The subsequent two- and three-body fragmentation processes are investigated using 3D-momenta coincident ion spectroscopy. The fragment angular distributions indicate a high probability for direct double-ionization to the "gateway states" to specific dissociation channels. Using *ab-initio* calculations, the electronic states of the molecular dication are identified; double-ionization from π-orbitals selectively triggers conformational rearrangement that depends upon the dication electronic state, which effectively acts as a gateway for H-migration and dissociation reaction pathways.

II. Site-selective dissociation upon core-electronic excitation in butadiene

Shabnam Oghbaie, Mathieu Gisselbrecht, Noelle Walsh, Bart Oostenrijk, Joakim Laksman, Erik P. Månsson, Anna Sankari, John H. D. Eland, and Stacey L. Sörensen
Submitted in Phys. Rev. Lett. (2017)

Soft X-rays were used to core excite butadiene to unoccupied π^* orbital. The

role of the initial charge localization was investigated by site-selective core-electron excitation. Dissociation channels identified in paper I are used to pinpoint the connection to symmetry breaking which is correlated to the core-hole localization. Using partly deuteriated d_4-butadiene, the site of terminal and central C-H bond dissociations are distinguished. The results show that the initial charge localization on the terminal carbon survives during autoionization and it enhances localized C-H(D) bond dissociation. The role of symmetry breaking on charge localization on the terminal carbon is reflected in the rate of H-migration and asymmetric dissociation.

III. Dissociation of cyclopropane in the double ionization continuum

Shabnam Oghbaie, Mathieu Gisselbrecht, Erik P. Månsson, Joakim Laksman, Christian Stråhlman, Anna Sankari, and Stacey L. Sörensen
To appear in Phys. Chem. Chem. Phys. (2017)

Tunable XUV-light was used to doubly ionize cyclopropane. Bond-selective dissociation in the ionization energy range of 25-35 eV has been investigated. With the aid of *ab initio* quantum calculations dication states and their favoured fragmentation pathways are determined, and compared with the experimental appearance energy and kinetic energy released of dissociation. The results confirm that sequential double ionization processes coupled via ring-opening nuclear motion lead to intense dissociation channels below the vertical double ionization potential. Dissociation channels appearing above the vertical double ionization threshold are preceded by double ionization processes predominantly within the Franck-Condon region populating excited dication states.

IV. Frequency tuning drives nuclear dynamics in carbon 1s excitation in cyclopropane

Shabnam Oghbaie, Mathieu Gisselbrecht, Joakim Laksman, Erik P. Månsson, Bart Oostenrijk, Noelle Walsh, Anna Sankari, and Stacey L. Sörensen
In manuscript

Soft X-rays were used for core-electron state-selective excitation of cyclopropane to different π^*, σ^* orbitals. Branching ratios of the dissociation channels identified in the paper III are measured using ion-ion coincidence mass-spectroscopy to pinpoint the connection between the anti-bonding character of the core-to-valence

excited states and Auger decay population of dissociation gateway states. The results indicates that the dissociation pattern changes in such a way that reflects the anti-bonding character of the core-excited states mainly remains during Auger decay thus populating repulsive states for the dissociation channels in the double ionization continuum.

V. Molecular dynamics of NH_3 induced by core-electron excitation

Noelle Walsh, Anna Sankari, Joakim Laksman, Tomas Andersson, Shabnam Oghbaie, Feras Afaneh, Erik P. Månsson, Mathieu Gisselbrecht and Stacey L. Sorensen
Phys. Chem. Chem. Phys., 17, 18944 (2015)

Soft X-rays were used for tuning the photon energy over ammonia N1s-$4a_1$ excitation. The angular distribution of two-body dissociation products is measured. The well-defined angular anisotropy of the fragment strongly changes as a function of the photon energy, which suggests a very rapid hydrogen atom motion changes the molecular geometry (from the pyramidal to the planar geometry) within a few femtosecond, *i.e.* during core-hole lifetime.

Contents

Chapter 1

Introduction

Absorption of light by molecules is a fundamentally important process for chemistry and biology, for planetary atmospheres and for energy conversion devices. The fate of a photoexcited molecule depends upon the energy of the photon, and upon the molecule and its environment. It is clear that photoabsorption puts the molecule in an unstable electronic state, and that the response is generally very rapid. This can take place in several ways: via electronic decay on the attosecond to femstosecond timescale [1, 2], via nuclear rearrangement (*e.g.,* isomerization and dissociation) on the femtosecond to microsecond time scale [3], or via optical emission (fluorescence) generally on nanosecond timescale [4]. One area of particular interest is to achieve "selectivity" in photochemical reactions [5, 6, 7]. Tuning the irradiating photon energy can potentially fulfil the "selectivity" criterium of light-driven chemical reactions [8, 9]. Using tunable synchrotron radiation in the soft x-ray range, a charge/hole can be localized at particular atomic sites in a molecule (by photoionization or photoexcitation). This initiates a process that can be monitored using spectroscopy that can image the temporal evolution of electronic and nuclear motion [10, 11, 12]. However, deeper insight into the temporal processes at the molecular level are necessary in order to take the advantage of the "selectivity" of the light-driven chemical reactions. This thesis also emphasizes the temporal perspectives, and addresses the questions of the timescale of different processes initiated by photoexcitation, in what order electronic and nuclear motion take place, and how they affect on each other?

There are relatively few classes of photochemical reactions governing biology and processes of importance in life science [13]. One of them, for instance, is *trans-cis* isomerization which is of critical importance to biology [7, 14, 15], which is also one of the subjects addressed in this work. Since isomerization occurs on the femtosecond

to picosecond timescale [15, 7], ultrafast time-resolved methods are necessary to follow the reaction in real time. Until recently, it has been a challenging task to directly determine the structure of molecules on ultrafast timescales. In this work, using a combination of advanced light sources and coincidence imaging spectrometry we are able to investigate the molecular dynamics coupled to site-selective excitation. For time-resolved measurements we take the advantage of a selectively populated electronic state with a few femtosecond lifetime as a clock for subsequent nuclear motions.

In particular, core-excited states in light elements decay preferentially via radiationless (Auger) decay, and these states are extremely short-lived [16, 17]. The short core-hole lifetime creates a situation where Auger decay competes with nuclear motion on the low femtosecond timescale. Chapter 2 covers the fundamental processes focusing on the photoabsorption and nuclear dynamics. Chapter 3 reviews the theoretical approximations for solving the Schrödinger equation for molecules that are implemented in the thesis and the computational methods employed in the calculations. Experimental methods and synchrotron radiation are discussed in Chapter 4, and results are presented in Chapter 5.

Chapter 2

Molecular interaction with photons

2.1 Photon-electron interaction

One of the most familiar light-matter interaction process is photoionization. Photoionization was initially discovered by Heinrich Hertz in 1887 [18] as the photoelectric effect, in which light irradiating metal leads to an electron ejection, the so-called photoelectron. At that time, the reason that low-frequency light does not cause electron emission while high-frequency light does, independent of the intensity of light, was incompatible with classical picture to scientists. In 1905 Einstein [19] provided an explanation based on Planck's constant, h, and the quantisation of electromagnetic radiation, in which the energy of the quanta is directly proportional to the frequency, $E = hv$. Einstein proposed the correlation between the photon energy, hv, and the kinetic energy, E_k, of the photoelectron by $W = hv - E_k$, where W is the work function *i.e.* the minimum energy required to remove an electron from the material.

For free molecules the picture of photoionization was further developed in 1934 by Koopmans' theorem [20] stating that the energy required to remove an electron from an orbital, on the assumption that the remaining electrons do not adjust their distributions, is the one-electron energy. Therefore, we may equate the one-electron orbital energy (or binding energy, E_B) with the ionization energy of the electron from that orbital, $E_I = E_B$. According to the molecular orbital (MO) theory [21], the molecular electronic wavefunction, Ψ_j, is constructed from Linear Combinations of constituent Atomic Orbitals (LCAO), $\Psi_j = \sum c_{ij}\psi_i$, where the c_{ij} coefficients are quantitatively calculated using the Hartree–Fock or self-consistent field (SCF) methods [for further information see section 3.1]. In the simplest case, when a single

photon gets absorbed by a molecule, the binding energy of the electron, and, as illustrated latter, bonding characteristic of the corresponding MO, can be determined by $E_B = hv - E_k$. This means that by exposing a molecule to tunable light we can ionize an electron or localize a hole/charge in different sub-shells of the molecule, and rearrange the atomic combination in different ways. The basic rule is that the lower binding energy electrons (valence electrons) of different atoms effectively overlap making chemical bonds between atoms, while the highest binding energy electrons (core electrons) do not overlap and remain localized on the constituent atoms. For instance, in butadiene combination of the four Cp_z atomic orbitals lying perpendicular to the (xy) molecular plane leads to creation of four π-symmetric MOs [see Fig. 2.1], with different bonding characteristics on terminal and central carbon-carbon bonds. The Highest Occupied Molecular Orbital (HOMO) is mostly localized on the terminal bonds, while the Lowest Unoccupied Molecular Orbital (LUMO) is mostly anti-bonding on these sites. The HOMO-1 is mostly localized on the central bond, while the LUMO+1 is mostly anti-bonding on this site. Therefore, ionization from the HOMO or electron excitation to the LUMO both reduce the bonding character of the terminal C=C bonds, and ionization from the HOMO-1 or excitation to the LUMO+1 both reduce the bonding character of the central C=C bond. Furthermore, due to the different chemical environments around the terminal and central sites, the terminal and central core electrons have different potential energies leading to the so-called chemical shift [22]. Thereby, using a tunable light source one can resonantly excite the core electrons from the terminal or central site into different unoccupied π-symmetric MOs, and manipulate both site-selective and bond-selective behaviour (e.g. dissociation).

2.1.1 Valence-electron ionization

In molecule the removal of valence electrons, which strongly contribute to chemical bonding, may result in the molecule breaking apart; however, manipulation of molecular bonds is not as simple as suggested by the MO picture of ionization. The significance of electron correlations on the hole/charge density and on molecular dissociation was illuminated in an experimental study of a peptide carbon-chain dissociation. The results show that just that after photoionization from a MO localized on one end of the chain, the molecule rapidly (within a few 100 fs) dissociates on the other end of the chain [11, 12]. Thereafter, this idea was inspired that by creation of a hole/charge in molecules, electronic correlation effects might trigger ultra-fast

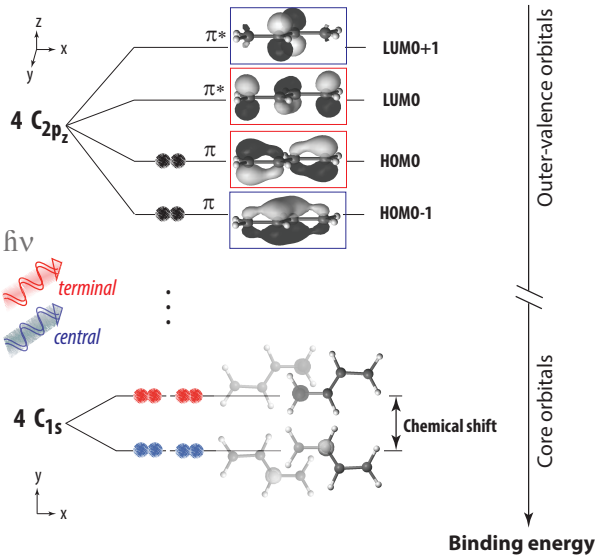

Figure 2.1: The π-symmetric molecular orbitals and chemically shifted core orbitals in butadiene. Depending on the energy of the incoming photon, we can either directly remove an electron from the valence orbitals or selectively excite a core electron from the chemically shifted terminal and central sites into unoccupied valence orbitals.

charge migration/oscillation through the electronic cloud of the molecule, which might erase the initial hole/charge localization at the time of molecular dissociation [23, 24, 25]. Recently, application of attosecond techniques on molecules offers the possibility of detecting ultra-fast charge-migration dynamics on a sub femtosecond timescale which is much shorter than the molecular vibrational response [26].

Long before these interpretations, evidence of electronic correlation effects have been observed in the photoelectron spectra of atoms. It was found that by internal relaxation upon single photoionization, as shown schematically in Fig. 2.2 (a), the internal energy is partitioned into multiple excitation and ionization, the so-called *satellite relaxation*: following inner-valence electron ionization due to the sudden change the remaining electrons do not have enough time to adjust themselves to the new energy states. Therefore, it is possible that, after the ionization of the first electron, another electron shakes to a higher orbital (*shake-up*) leading to two-hole one-particle M^{+*} electronic configurations [27] or into the continuum (*shake-off*) leading to two-hole M^{++} electronic configurations [2] [see Fig. 2.2 (a)]. The basic rule is that if the electron correlation effects are weak, as is often the case for outer-valence electrons, the MO picture of ionization fits the photoelectron spectrum well, including distinct main lines corresponding to one-hole electronic configurations; and if electron correlation effects are strong, as is typically the case for inner-valence electrons, the MO picture of ionization breaks down and the photoelectron spectrum represents a continuous series of m-hole n-particle *satellite* lines, indicating ultra-fast hole/charge migration through the system. For instance, in Fig. 2.3 (a) the photoelectron spectrum of butadiene measured at 280 eV photon energy is compared

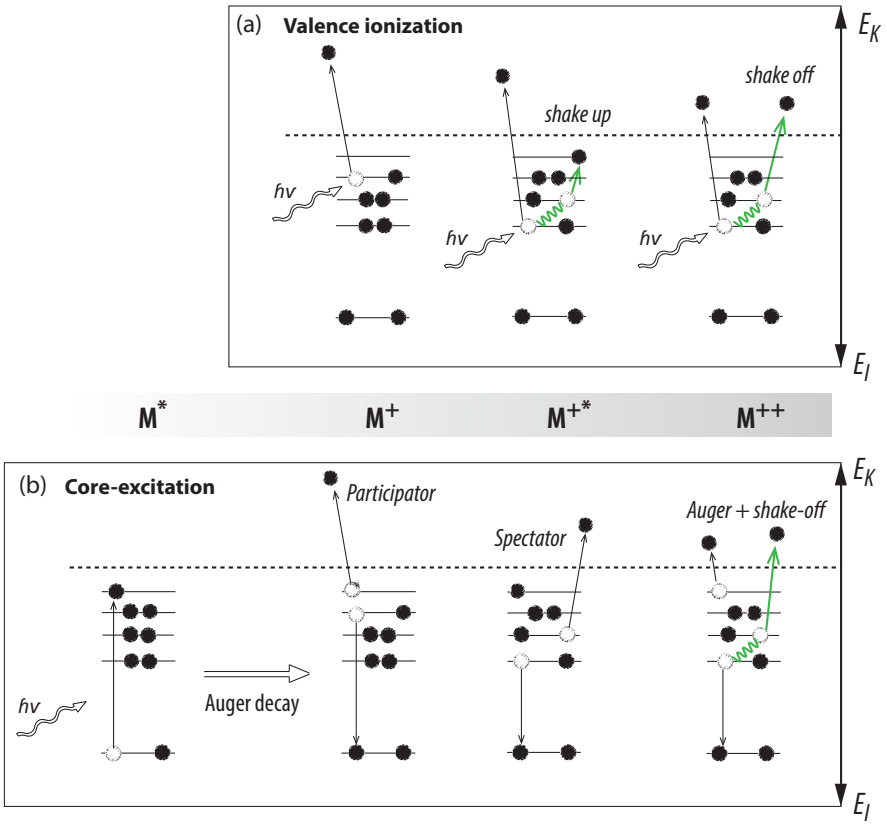

Figure 2.2: Schematic diagram shows different internal electronic relaxation processes following valence ionization (a) and core-electron excitation (b). The valence ionization may coincide with *shake-up* to two-hole one-particle M^{*+} states with another excited electron or with *shake-off* to two-hole M^{++} states with another ionized electron (a). The core-excitation follows by Auger decay (b). The exciting electron might participate in the decay leads to population of one-hole M^{+} states or stays as a spectator leads to population of two-hole one-particle M^{*+} states. Auger decay accompanied with a *shake-off* process leads to two-hole M^{++} final states.

with the MO picture of ionization. The comparison, to a great extent, correlates the photoelectron peaks to the ionized states with a vacancy in the molecular orbitals. However, for higher energy states the shape of the peaks converge to a broad Lorentzian-type, which according to the Cederbaum *et al.* [25] is an evidence of the breakdown phenomenon of the MO picture of ionization.

2.1.2 Core-electron excitation

One approach to site-selective localization of a hole/charge in molecules is core electron excitation or ionization. Due to the atomic character of the core electrons in molecules the creation of a core-hole should not drive any hole/charge migration

by itself. However, due to the increased nuclear charge on the valence electrons, the core-hole is rapidly (in a few femtosecond) filled by a valence-electron and the released energy of the core-hole filling is transferred to other valence electrons leading to "autoionization", via so-called Auger decay[1], populating singly and doubly ionized states [29, 1]. In general, the core-hole lifetime (Γ) is determined by partial Auger decay cross-section in terms of Coulomb matrix elements of the form:

$$\Gamma \propto < \Psi_{v_1} \Psi_{v_2} \mid \widehat{e^2/r_{12}} \mid \Psi_{core} \Psi_{continuum} > \tag{2.1}$$

where the rate of core-hole filling, $\Psi_{v_1} \longrightarrow \Psi_{core}$, depends significantly on the overlap between the valence and core electron wavefunctions, and thus, on the electron density around the initially excited atom. This has been experimentally confirmed for fluoromethane molecules (CH_xF_y) and generally in molecules with electronegative ligands, in which lifetime broadening of the C1s photoelectron dramatically decreases with increasing number of electronegative atoms [30, 31, 32]. However, in order to properly describe the degree of localization of the final states electron correlation effects must also be considered in autoionization of valence electrons, $\Psi_{v_2} \longrightarrow \Psi_{continuum}$, which may obscure the role of the initial core-hole localization on the final-state population [33].

Auger decay can be separated into *participator* and *spectator*. These processes are shown schematically in Fig. 2.2 (b). *Participator* Auger decay might lead to one-hole configuration M^+, identical to the states populated by direct valence ionization. The spectral weights of core-hole final states are, however, different than those created by direct valence ionization because the initial state is different and the deexcitation is driven by the Coulomb operator, rather than the dipole operator which governs the direct ionization process. In *spectator* Auger decay the excited electron is not involved but remains a spectator and two other (valence) electrons take part in the decay. Thus, this process leads to two-hole one-particle M^{*+} final states, identical to the *shake-up* final states shown in Fig. 2.2 (a).

An illustrative example is butadiene, where localized Auger decay can be studied by comparison of the Auger decay of the terminal and central carbon core holes. In Fig. 2.3 (b) photoemission after the terminal and central C1s-π^* resonance excitations is monitored. The localized core-hole filling is mostly reflected in the population

[1] Core-hole vacancies in molecules decay on an ultra-fast timescale by fluorescence or radiationless Auger decay. In general, for low energy transitions, e.g., light elements or high-lying inner-shells in heavier elements, Auger decay is the dominant (98.99%) relaxation process [28] and occurs on a timescale of 10^{-15} to 10^{-14} s.

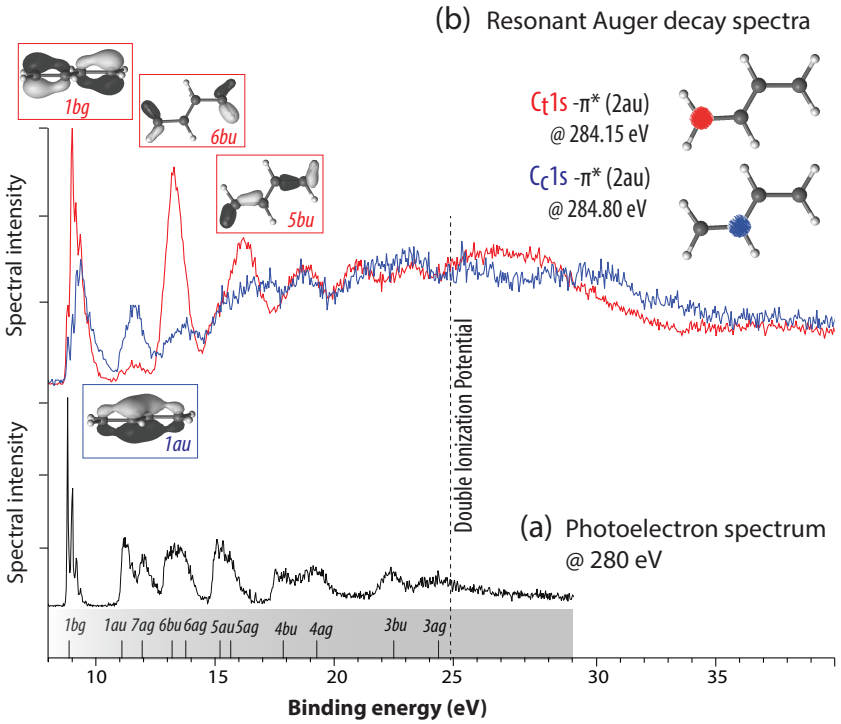

Figure 2.3: Photoelectron spectrum of butadiene measured at 280 eV photon energy is shown with the calculated MO energies at the level of cc-pVTZ basis set (a). MO nomenclature is based on the molecular symmetry and the irreproducible representations of the C_{2h} point group to which the equilibrium geometry of butadiene belongs. Resonant Auger spectra measured upon terminal and central C1s to π^* excitation (b). The localized character of the core-hole filling is well reflected on the rate of Auger decay populating one-hole final states.

of one-hole final states: the rate of Auger decay leading to ionization of $1b_g$ orbital (mostly making terminal C=C bonds), $6b_u$ orbital (making terminal C-H bonds), and $5b_u$ orbital (making terminal C=C and C-H bonds) is enhanced after terminal C1s excitation, and rate of Auger decay leading to ionization of $1a_u$ orbital (mostly making central C=C bond) is enhanced after central C1s excitation. The localization effect and hole vacancy is not easy to detect when higher binding energy electrons contribute to the Auger decay. In paper II the degree of localization in Auger decay to double ionization continuum is studied using ion-ion coincidence measurements.

2.2 Electronic predetermination of nuclear motion

One of the main questions to address in this thesis is to what extent electronic processes can influence or determine molecular dissociation. An important condition

that makes the relationship between the electronic state of a molecule and its geometry meaningful is the Born-Oppenheimer approximation [34]. It states that motion of the electrons are much faster than motion of the nuclei, justified by thousand times lighter mass of electron, and can be decoupled: $\Psi_{tot}(\overrightarrow{r_i};\overrightarrow{R_i}) = \Psi_{elec}(\overrightarrow{r_i};\overrightarrow{R_i})\Psi_{nucl}(\overrightarrow{R_i})$, where r_i stands for electronic coordinates and R_i for nuclear coordinates. This approximation simplifies the application of the Schrödinger equation to molecules, $H\Psi(\overrightarrow{r_i};\overrightarrow{R_i}) = E\Psi(\overrightarrow{r_i};\overrightarrow{R_i})$, where electronic energy is determined by the chosen coordinate R of the nuclei and varying the coordinate R in small steps and repeatedly solving the electronic Schrödinger equation. Since the procedure of recalculating the potential energy as a function of nuclear coordinates is reminiscent of the conditions for the adiabatic theorem, this manner of obtaining a potential energy surface (PES) is often referred to as the adiabatic approximation, and the PES itself is called an adiabatic surface.

In general, in order to study the evolution of the nuclear geometry on an electronic state, geometry optimization calculation over all degrees of freedom of molecule is required [for further information see section 3.2]. For a (non-linear) molecule consist of N atoms, nuclear motion is described by the derivatives of the multidimensional PES[2] along 3N-6 nuclear coordinates, known as vibrational normal mode (*e.g.* stretching, bending, torsion, etc.). For molecules consisting of more than three atoms (>3 vibrational modes), dissociation is most likely preceded by isomerization processes, where a mixture of different vibrational modes leads to rearrangement into another molecule which has exactly the same atoms, *e.g.* conformational *trans* to *cis* rearrangement, hydrogen migration in unsaturated hydrocarbons (CH_2=CH-R $\leftrightarrow$ CH_3-C=R$^\bullet$) replacing order of π-bonds, or ring-deformation in cycloalkanes, etc. In general, the key to controlling dissociation and accompanying isomerization processes in molecular ions is to prepare them in specific electronic states from which the reaction proceeds through a desired pathway on multidimensional PESs towards a certain set of final fragment products. This interpretation, based on the Born-Oppenheimer approximation, however, fails when nuclei move as fast as electrons. This can happen when electronic states are close enough to vibronically interact with or cross each other, a situation known as a conical intersection (CI) [see Fig. 2.4 (b)], and non-adiabatic behaviour of internal energy relaxation occurs through subtle correlated electronic and nuclear motions. The failure of the Born-Oppenheimer

[2]The PES might define the energy as a function of one or more coordinates; if there is only one coordinate, the surface is called a potential energy curve, and if there are two coordinates, the surface is called a landscape.

approximation can also happen following core-electron excitation (ionization) where ultrafast nuclear motion (in particular for low-mass hydrogen atoms) takes place prior to Auger decay, *i.e.* in a few femtoseconds [35, 36]. In this thesis, we mostly focus on the non-adiabatic processes of molecules acting as key to controlling dissociation dynamics.

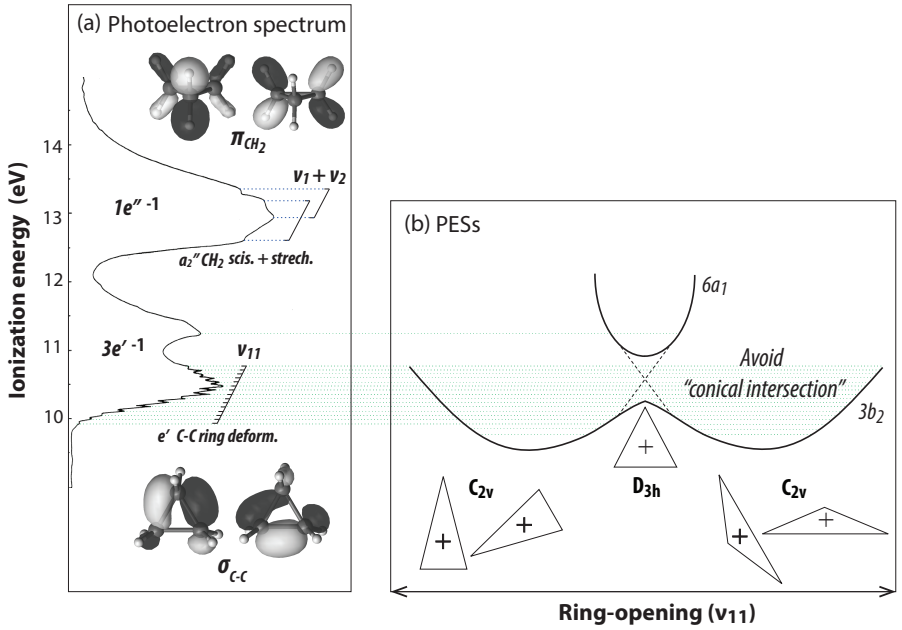

Figure 2.4: Photoelectron spectrum of cyclopropane (a) taken from ref [37]. Jahn-Teller splitting of the orbitally degenerate $3e'^{-1}$ states along symmetry breaking e'-ring deformation (v_{11}) is visible. In the adiabatic representation of PESs along the ring-opening coordinates avoided crossing at the geometry of D_{3h} symmetry creates two states of C_{2v} symmetry (b).

2.2.1 Jahn-Teller Symmetry breaking

In 1937, Hermann Jahn and Edward Teller postulated a theorem [38] stating that "stability and degeneracy are not possible simultaneously unless the molecule is a linear one" in regards to its electronic state. This implies that preparing a nonlinear molecule in a spatially degenerate electronic state causes the molecule to distort spontaneously in such a way that the degeneracy is lifted and a new equilibrium structure of lower symmetry is attained. The well-known example of Jahn-Teller distortion occurs in cyclopropane [39]. The MO sequence of cyclopropane can be written as $(1a_1'^2)$ $\underline{(1e'^2 1e'^2)}$ $(2a_1'^2)$ $\underline{(2e'^2 2e'^2)}$ $(1a_2''^2)$ $(3a_1'^2)$ $\underline{(1e''^2 1e''^2)}$ $\underline{(3e'^2 3e'^2)}$ $(2a_2'')(1a_2')$ $\underline{(4e'4e')}$ $\underline{(5e'5e')}$. The Jahn-Teller instability is created by ionization (excitation) of occupied degenerate orbitals, and also by electron excitation to unoccupied degener-

ate orbitals. For instance, photoionization of the two outer-most doubly degenerate 3e′ (σ_{C-C}) and 1e'' (π_{CH_2}) orbitals are studied in the photoelectron spectrum [37] shown in Fig. 2.4 (a). Due to the large amount of ring strain in the triangular carbon structure of D_{3h} symmetry an effective Jahn-Teller distortion occurs upon ionization of 3e′, while no evidence of splitting is seen upon the 1e'' ionization. The extensive association of the first Jahn-Teller component of the $3e'^{-1}$ band with the C-C ring-deformation ν_{11} vibrational mode indicates the internal energy releasing pathway of $3e'^{-1}$ ionization. Theoretically two equally minimized energy pathways were revealed for the $3e'^{-1}$ states, as the adiabatic representation of PESs are shown in Fig. 2.4 (b), where the geometry of D_{3h} symmetry distorts either by one elongated C-C bond or by two elongated C-C bond leading to two geometries of C_{2v} symmetry. In papers III and IV the Jahn-Teller instability of cyclopropane following double ionization and core-electron excitation is addressed as a key factor to controlling subsequent dissociation dynamics.

2.2.2 Symmetry breaking upon core-hole localization

The process of a local excitation through promotion of a core electron to an unoccupied valence orbital often leads to rapid nuclear geometry change [40]. This is due to the sudden change in potential that leads to different equilibrium geometry in core-excited states. Nuclear geometry change upon core-electron excitation (or ionization) can be predicted using the *equivalent core* "Z+1" model [41, 42]. The underlying picture of the model is straightforward. The removal of a core electron in an atom with nuclear charge "Z" effectively increases the nuclear charge "seen" by the valence electrons. For these electrons, the core of the ion is nearly identical to that of the neutral atom but with a nuclear charge "Z+1".

In molecules of equivalent core-level sites, proceeding via symmetry breaking nuclear motion is essential for core-hole localization. An illustrative example is butadiene with the two equivalent terminal carbons chemically shifted from the two equivalent central carbons. According to the "Z+1" model, the equilibrium geometry of the terminal carbon C1s to π^* excitation, represented by the equilibrium geometry of neutral $NH_2CHCHCH_2$, differs from the equilibrium geometry of the central carbon C1s to π^* excitation, represented by the equilibrium geometry of neutral $CH_2NHCHCH_2$. Using geometry optimization calculation the equilibrium geometries are obtained with bent geometries where adjacent hydrogen atoms connected to the excited atom place out of the molecular plane. A schematic cut through the

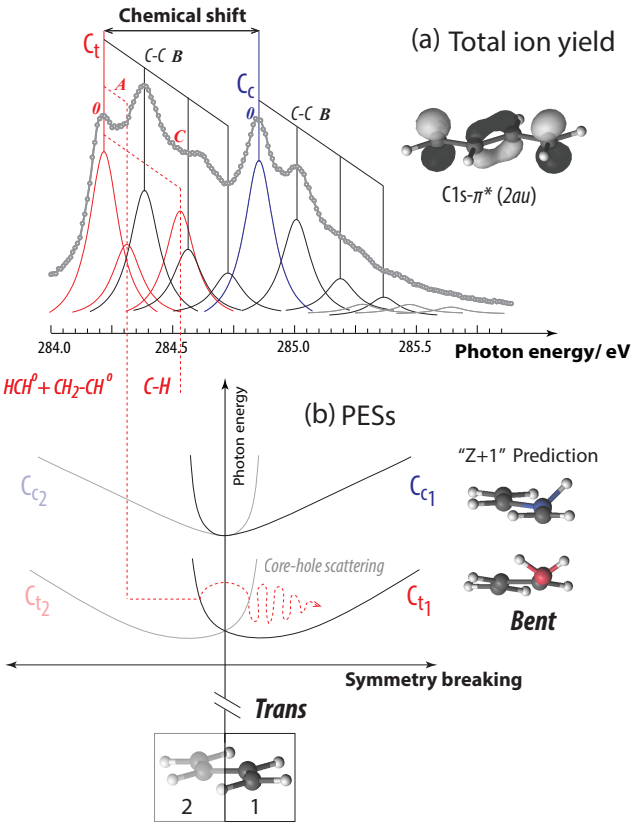

Figure 2.5: Total ion yield spectrum of butadiene for C1s excitation to $\pi^*(2a_u)$ (a). The vibrational contributions are fitted using a Voigt function. A cut through PES of terminal and central core-excited states are calculated using "Z+1" approximation (b), with bent equilibrium geometries for th ecore-excited states. Promotion of C1s from chemically shifted terminal and central sites of butadiene leads to two doubly degenerate core-excited states separated along the symmetry breaking nuclear motion.

PESs of the terminal and central core-hole states along the out-of-plane symmetry breaking coordinate are shown in Fig. 2.5 (b), suggesting that symmetry breaking occurs to a greater extent upon terminal core-hole localization. This is justified, based upon the bonding characteristics of the π^* orbital (LUMO), which is antibonding on the terminal and bonding on the central site. Provided that nuclear evolution occurs within the core-hole lifetime, it can effectively localize the core hole during subsequent Auger decay and potentially increases control of subsequent dissociation. Although a few femtosecond lifetime of the butadiene core-excited states is enough for light mass of hydrogen atom to initiate motion (H-atom migration in hydrocarbons typically occurs on a few tens of femtosecond [43]), it prohibits the symmetry-broken system to reach the equilibrium geometry. However, comparison of the resonant Auger spectra upon terminal and central core electron excitation [see Fig. 2.3 (b)] shows that the memory of core-hole localization during Auger decay is retained to a greater extent for terminal carbon excitation, which might pinpoint the role of symmetry breaking on "degree of localization" in Auger decay, which is the subject of paper II.

Probing PES

One approach to study the potential energy surface of a core-excited state is by tuning the photon energy over the electronic transitions and collecting all of the ions or electrons. In Fig. 2.5 (a) total ion yield[3] spectrum of C1s to $(2a_u)\pi^*$ excitation of butadiene is shown. The spectrum shows a 0.64 eV chemical shift between the terminal and central C1s excitation. The vibrational features associated in the terminal and central excitation are indicated using the Voigt (Lorentzian+Gaussian) profile fitting. The vibrational excitation on both sites mostly correspond to the in-plane C-C stretching modes (B), however, upon terminal excitation a C-H stretching vibration (C) with 375-385 meV energy and a weak out-of-plane (HCH bending+CH_2-CH torsional) vibration (A) with 100-120 meV energy also contribute to the spectrum, in analogy with vibrational excitation in ethylene C1s to π^* excitation [36].

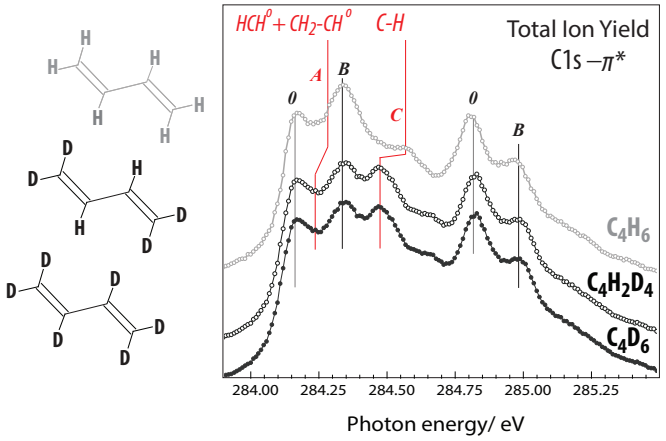

Figure 2.6: Total ion yield spectra of C_4H_6, $C_4H_2D_6$, and C_4D_6 for C1s excitation to $\pi^*(2a_u)$.

One way of unambiguously distinguishing vibrational excitation of the C-H group from those of the C-C group is to compare TIY spectra of C_4H_6 sample with the deuterium labelled samples C_4D_6, and $C_4H_2D_4$. As shown in Fig. 2.6, due to the heavier mass of deuterium atom the features C and A are shifted towards lower energies in the deuteriated samples, while the energy of feature B for all species is unchanged. The spectra of C_4H_6 and C_4D_6 show no difference in vibrational excitation of C_C1s to π^* transition suggesting that there is no C-H vibration associated with the C_C1s to π^* resonance, and identical spectra recorded for C_4D_6 and $C_4H_2D_4$ (where deuterium atoms bonded to C_T and hydrogen atoms bonded to C_C) suggesting that the C-H vibrational excitation of the C1s to π^* resonance only arises from the terminal

[3]The core excited state decays rapidly via Auger decay populating ionized-electronic states, thus, the total electron yield spectrum is essentially equivalent to the absorption spectrum below the C 1s ionization potential.

sites. The different vibrational excitation is consistent with the prediction from the "Z+1" approximation, and different Auger decay spectra following terminal and central C1s excitation. Regarding the bonding character of the π^* orbital on the central bond and the anti-bonding character on the terminal bonds, the frequency of transition between planar geometry to the bent geometry (along CH_2 twisting/bending) increases upon terminal C1s excitation to the π^* state. In paper II, by comparison of the dissociation patterns upon terminal and central core excitation, the role of symmetry breaking on the subsequent dissociation is investigated.

2.2.3 Molecular-frame angular distribution

The dissociation axes of molecules in gas phase are of course randomly oriented; however, if an electronic transition occurs via a linearly (highly) polarized light molecules of specific orientation undergo dissociation, which leads to anisotropic fragment angular distribution, containing femtosecond molecular dynamics. This is due to the spatial-selectivity inherent to the transition dipole moment, where within the dipole approximation the maximum interaction occurs when polarization vector of the light, $\overrightarrow{\epsilon}$, is aligned with the transition dipole moment, $\overrightarrow{\mu}.\overrightarrow{\epsilon} \propto cos(\theta)$ [44]. According to Fermi's Golden Rule, the probability for an electronic transition is defined by the dipole matrix element, $P_{if} \propto | < \Psi_{e,f} \mid \overrightarrow{\mu}.\overrightarrow{\epsilon} \mid \Psi_{e,i} > |^2$, which is determined by electronic wavefunctions of the initial and final states.

No spatial-selectivity (unless achieved by vibronic coupling)

Character table

D3h	E	2C3	3C'2	σh	2S3	3σv	linear, rotations	quadratic
A'1	1	1	1	1	1	1		x2+y2, z2
→ A'2	1	1	-1	1	1	-1	Rz	
→ E'	2	-1	0	2	-1	0	(x, y)	(x2-y2, xy)
A"1	1	1	1	-1	-1	-1		
→ A"2	1	1	-1	-1	-1	1	z	
E"	2	-1	0	-2	1	0	(Rx, Ry)	(xz, yz)

Product table

D3h	A'1	A'2	E'	A"1	A"2	E"
A'1	A'1	A'2	E'	A"1	A"2	E"
→ A'2	A'2	A'1	E'	A"2	A"1	E"
→ E'	E'	E'	A'1+A'2+E'	E"	E'	A"1+A"2+E"
A"1	A"1	A"2	E"	A'1	A'2	E'
→ A"2	A"2	A"1	E"	A'2	A'1	E'
E"	E"	E"	A"1+A"2+E"	E'	E'	A'1+A'2+E'

Table 2.1: Character table and product table of D_{3h} point group.

The most elegant way to find the transition probability is using the fact that molecular orbitals are constructed according to specific symmetries (in the irreducible representation of the point group to which the molecules belong), and the fact that for an electronic transition to be allowed, the dipole matrix element must be non-zero. Thus, the total symmetry of $\mu_\alpha = \Psi_i \otimes \alpha \otimes \Psi_f$ has to span the totally symmetric representation of the point group to which the molecules belong, otherwise the transition is forbidden. We use cyclopropane C1s excitation to different valence

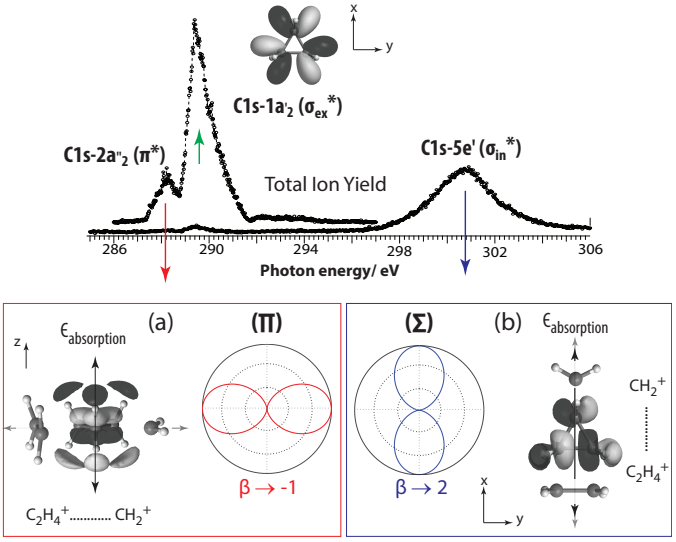

Figure 2.7: TIY spectrum covering C1s to π^* and σ^* transitions in cyclopropane. Molecular alignment and anisotropy distribution of dissociation with respect to the polarization vector of the linearly polarized light following C1s$\rightarrow$ $2a_2''$ (a) and cyclopropane C1s$\rightarrow$ $5e'$ (b) excitation.

orbitals to exemplify how the character table of a molecule is used to determine the molecular frame of photo-absorption. Since the 1s orbital is totally symmetric the spatial selectivity is determined by the symmetry of the valence orbital. The symmetry (linear/quadratic coordinate) properties of the molecular orbitals exist in the irreducible representations [see Table. 2.1]. In the TIY spectrum of cyclopropane over C1s excitation shown in Fig. 2.7 three resonance features are seen: one corresponding to Π symmetric C1s$\rightarrow$ $2a_2''$ excitation, and two corresponding to Σ symmetric C1s$\rightarrow$$1a_2'$ and C1s$\rightarrow$$5e'$ excitations. In cyclopropane, with equilibrium geometry of D_{3h} symmetry, C1s excitation to $2a_2''$ orbital (with linear coordinate along z axis) occurs predominantly with the z-components of the dipole matrix element, where $\underline{\mu_z} = A_1' \otimes \underline{A_2''} \otimes A_2'' = A_1'$ [see Fig. 2.7 (a)], and C1s excitation to $5e'$ orbital (with linear coordinate along x-y axes) occurs predominantly with the x(y)-components of the dipole matrix element, where $\underline{\mu_{x(y)}} = A_1' \otimes \underline{E'} \otimes E' = A_1' + A_2' + E'$ [see Fig. 2.7 (b)]. However, in C1s excitation to the symmetric $1a_2'$ orbital (without linear and quadratic coordinates), the dipole matrix element is not directed and spatial-selectivity is provided only by instantaneous symmetry breaking. In cyclopropane the three degenerate C1s leads to three degenerate C1s-$1a_2'$ states, which in turn can be coupled through the Jahn-Teller active ring-deformation vibrational mode e', where $\underline{\mu_{x(y)}} = (A_1' \otimes \underline{E'} \otimes A_2') \otimes E' = A_1' + A_2' + E'$, and causes the transition to occur predominantly with the x(or y)-components of the dipole matrix

element.

The formalism for photo-fragment angular distribution in spherically symmetric systems has been developed by Zare *et al* [45, 46]: within the dipole approximation, the angular distribution of emitted particles with respect to the polarization vector of the light is expressed by $I(\theta) \propto 1+\beta\ (3\cos^2\theta\ -1)/2$, which is parametrized by the anisotropy value, β, ranging from 2 to -1. The β value of a dissociation predicted by the spatial-selectivity of the electronic transition and associated vibrational motion, can be extracted from the fragment's angular distribution if molecular dissociation takes place rapidly enough, *i.e.* faster than molecular rotations (known as axial recoil approximation)[46]. Regarding rapid dissociation of cyclopropane into $CH_2^+/C_2H_4^+$ ion pair, dissociation following C1s to π^* ($2a_2''$) excitation leads to $\beta \to -1$ [see the red curve in Fig. 2.7 (a)], and dissociation following C1s to σ^* ($5e'$) excitation leads to $\beta \to 2$ [see the blue curve in Fig. 2.7 (b)].

Chapter 3

Molecular quantum calculation

In the following chapter the *ab-initio* quantum calculation methods implemented in this research are reviewed. The main starting point in calculating molecular electronic wavefunction is the Hartree-fock (HF) method. Multi configurational (MC) methods that take electron correlation effects into account, when calculating molecular non-stationary (excited, bond-breaking,...) states, are discussed next. Finally geometry optimization and density functional theory are reviewed.

3.1 Electronic optimization

The main goal of computational techniques is to approximately solve the non-relativistic time independent Schroedinger equation for many electron systems. Considering the Born-Oppenheimer approximation and solving the electronic equation $H\psi(r;R) = E(R)\psi(r;R)$, the simplest Hamiltonian (H) for a n-electron system is achieved within the mean field approximation [47], where a single electron moves in a mean potential field of the n-1 remaining electrons and the N nuclei of a given molecular system, the so-called Hartree-Fock (HF) method [48]:

$$H = -\sum_i^n \frac{1}{2}{\nabla_i}^2 + \sum_i^n \sum_I^N \frac{Z_I}{r_i R_I} - \sum_{ij}^n \frac{1}{r_{ij}} \tag{3.1}$$

where the first term describes kinetic energies of n electrons in the system and the last two terms describe the Coulomb interactions between electron-nucleus and electron-electron respectively. In other words, the electronic wave function $\psi(r;R)$ in molecules describes the distribution of all the electrons in the presence of the potential field created by the fixed nuclei.

3.1.1 Basis-set

The starting point for the HF method is a set of approximate one-electron wave functions known as basis-set. For an atomic orbital calculation these are typically the orbitals for a hydrogenic atom χ_i, given by a single-electron Slater-Type Orbitals (STOs), known as spin orbital[1] [49]. For a molecular orbital calculation the initial approximate one-electron wave functions are typically a linear combination of atomic (Slater-type) orbitals (LCAO), $\psi_i = \Sigma c_i \chi_i$. In practice, the STOs are computationally difficult and could instead be approximated as linear combinations of Gaussian orbitals instead [50]. The minimal basis set is STO-nG, where n represents the number of Gaussian primitive functions comprising a single basis function. These minimal basis sets, however, are not flexible enough to describe valence electrons taking part in chemical bonds and for presenting the deformation several different types of extended basis sets are required. In split-valence basis set multiple functions are used to represent each orbital, which can instead be composed of a fixed linear combination of primitive Gaussian functions. For example, the 2s atomic orbital is expressed as the sum of two STOs, $\chi_{2s} = \chi_{2s}^{STO}(r_1, \zeta_1) + d\chi_{2s}^{STO}(r_2, \zeta_2)$, where the ζ value accounts for the size of orbital, and the constant d determines how much each STO will contribute to the final orbital. The triple and quadruple-zeta basis sets work the same way, except they use three and four Slater equations instead of two[2]. Since the different orbitals of the split have different spatial extents, the combination of two allows the electron density to adjust its spatial extent according to the particular molecular environment. In order to get closer to the exact electronic energy, and to better represent electron density in bonding regions polarization and diffuse functions are also added to the basis set by which molecular orbitals are allowed to be more asymmetric and far from the nucleus [3]. For example, regarding hydrogen atom involved in a bond in a molecule (like the C-H bond in hydrocarbons), the electron density is no longer spherical s-type orbital and an addition of a p-type

[1] which satisfies anti-symmetry requirements and consequently the Pauli principle by changing sign upon exchange of two electrons.

[2] The notation for the split-valence basis sets came from the group of John Pople and is typically n-ijG or n-ijkG [50], where n is number of primitives for the inner shells; ij or ijk are number of primitives for contractions in the valence shell. The ij notations describes sets of valence double zeta quality and ijk sets of valence triple zeta quality.

[3] The polarization functions are denoted in Pople's sets by an asterisk. The most used Pople's basis set is 6-31G* (defined for the atoms H through Zn) which is a valence double-zeta polarized basis set that adds to the 6-31G set six d-type Cartesian-Gaussian polarization functions on each of the atoms Li through Ca and ten f-type Cartesian Gaussian polarization functions on each of the atoms Sc through Zn. The main disadvantage of Pople's basis sets is that they do not converge towards a basis set limit with increasing size.

orbital to the existing s-type orbital in a hydrogen atom will shift (or polarize) it, so that it lies more along the C-H bond. For carbon atom adding d-type and f-type basis functions would be considered to be polarization functions. In general, to polarize a basis function with angular momentum l, mix it with basis functions of angular momentum $l + 1$. Widely used basis sets are those developed by Dunning and co [51], which are also used in this work. These basis sets have become the current state of the art for quantum calculation of molecular states since they are designed to converge systematically to the complete-basis-set (CBS) limit using empirical extrapolation techniques. For first- and second-row atoms, the basis sets are "aug-cc-pVNZ" where N=D,T,Q,5,6,... (D=double-zeta, T=triple-zeta, etc.). The "cc-p", stands for "correlation consistent polarized" and the "V" indicates they are valence only basis sets. They include successively larger shells of polarization (correlating) functions (d, f, g, etc.). The prefix "aug" means that the basis is augmented with diffuse functions.

3.1.2 Self Consistent Field (SCF)

In the calculation of molecular orbitals $\psi_i = \Sigma c_i \chi_i$ the c_i coefficients are optimized within the variational principle and secular equation [52]. The variational principle states that for a time-independent H operator, any trial wave function will have an energy expectation value that is greater than or equal to the true ground state wave function corresponding to the given H[4]. The resultant variational conditions on minimizing the molecular orbital energy lead to a new one-electron operator, the Fock operator (F),

$$F_i \psi_i = (H^{core} + \Sigma_i^{n/2}[2J_j - K_j])\psi_i = E_i \psi_i \tag{3.3}$$

where the H core contributes to kinetic energies of n-electrons and electron-nucleus Coulomb interaction, J and K are direct and indirect/exchange Coulomb operators respectively, where K describes a certain correlation effect between electrons with parallel spin. Since the F operator depends on the orbitals used to construct the

[4]For a hamiltonian H that describes the studied system and any normalizable function Ψ with arguments appropriate for the unknown wave function of the system, we define the functional

$$\epsilon\Psi = \frac{\langle\Psi|H|\Psi\rangle}{\langle\Psi|\Psi\rangle} \tag{3.2}$$

the $\epsilon \geq E_0$ where E_0 is the lowest energy eigenstate (ground state) of the Hamiltonian, and $\epsilon = E_0$ if and only if Ψ is exactly equal to the wave function of the ground state of the studied system.

corresponding F matrix, the eigenfunctions of the F operator are then new orbitals which can be used to construct a new F operator. In this way, the HF orbitals are optimized iteratively until the change in total electronic energy falls below a predefined threshold. Ultimately, a set of self-consistent field (SCF) one-electron orbitals are calculated. This method is also knows as *ab-initio* calculation.

3.1.3 Electronic correlation

The best energies obtained at the Hartree-Fock level are still not accurate, since they use a mean field potential for the electron-electron interactions. Because electrons interact and repel each other, their motion in atoms is correlated. Thus, consideration of electronic correlation effects is mostly essential for calculating non-stationary states, *e.g.* bond breaking, transition states, and conical intersections, where two or several electronic configurations are near or degenerate. The method for adjusting the molecular wavefunctions for electron correlation is configuration interaction (CI) [53]. In this method the molecular wavefunction is defined as a linear combination of configuration state functions (CSFs) (Slater determinant), $\Psi = \Sigma_n C_n \psi_n = C_{HF}\psi_{HF} + C_{ex1}\psi_{ex1} + C_{ex2}\psi_{ex2} + ...$, where the first term is normally the Hartree–Fock determinant, and other (single, double,..) excitation determinants can be characterized by the number of spin orbitals that are swapped with virtual orbitals from the Hartree–Fock determinant. An accurate wavefunction often requires a large number of configurations [54]. This is due to poor representation of the virtual space, which is the major problem in applying the full-CI procedure to large molecules. On the other hand, excitation energies of truncated CI methods are generally too high, because the excited states are not as well described as the ground state is. For equal (balanced) correlation of ground and excited states (better excitation energies) one can use more than one reference determinant from which all excited determinants are included (multireference configuration interaction). The most promising approach is the multiconfiguration self-consistent field (MCSCF) method [55]. The MCSCF method goes beyond the CI method by variationally optimizing the orbitals simultaneously with the mixing coefficients, in which the set of coefficients of both the CSFs and the basis functions in the molecular orbitals are varied to obtain the total electronic wavefunction with the lowest possible energy. This method can be considered a combination between configuration interaction (where the molecular orbitals are not varied but the expansion of the wave function are) and Hartree–Fock (where there is only one determinant but the molecular orbitals are varied), by which the

expectation value of the total energy is variationally stationary with respect to all variations of the coefficients and the orbitals. A particularly important MCSCF approach is the complete active space (CAS) method (CASSCF) [56]. The CASSCF wave function is formed from a complete distribution of a number of active electrons in a set of active orbitals, which in general constitute a subset of the total occupied space.

Whilst the CASSCF wavefunction describes all needed static correlation effects, dealing with the strongly correlated systems, dynamic correlation effects are required to achieve accurate energy levels. Dynamics correlation effects can be added on top of CASSCF using Rayleigh-Schrödinger theory. The CASPT$_2$ method perturbatively computes the dynamic correlation effects using a formalism that employs single or multi (in the case of degenerate electronic states of the same symmetry) CASSCF reference states and partitioning of the Hamiltonian into a zero-order part and the perturbation part, $H = H_0 + V$ [57] [5].

The major drawback of the CASSCF approach is that the number of configuration state functions (CSFs) increases steeply by the binomial coefficient of electrons in the active orbitals. For example, distributing 12 electrons among 12 active orbitals yields 226512 singlet CSF's, if no reduction due to spatial symmetry is assumed. Adding one more active orbital increases the number to 736164. This strong dependence of the size of the MC expansion on the number of active orbitals makes it difficult to perform CASSCF calculation with more than around 12 active orbitals, at least in cases where the number of active electrons is about the same as the number of active orbitals. In most applications this limit does not impose a problem, but there are situations where the ability to increase the number of correlating orbitals in the MCSCF wave function is desirable. One way to solve this problem is to restrict the number of electrons in certain subspaces, which was done in the restricted active space SCF method (RASSCF) [58]. A restricted active space (RAS) is used, where the active orbitals are partitioned into three subsets: RASl,

[5] In the second order perturbation theory configuration space is generated by iteratively solving a set of Rayleigh-Schroedinger equations, $(H_0 - E_0)\psi_1 = V\psi_0$, until one reaches a diagonal zero-order Hamiltonian H_0. The zero-order Hamiltonian is written as a sum of projections of a one-electron Fock operator onto the reference function P_0 and its orthogonal interacting configuration space P_I, $H_0 = P_0FP_0 + P_IFP_I$. Fock operator is generalized with $F = \Sigma_{p,q} f_{pq} E_{pq}$ and $f_{pq} = h_{pq} + \Sigma_{r,s}[(pq|rs) - 1(pr|qs)/2]$, where E_{pq} operator removes an electron from orbital q and places it in orbital p. One or two of the indices (p,q,r,s) must be outside the active space. In double occupied p orbital $f_{pp} = -IP_p$ is Ionization Potential, and for unoccupied orbital $f_{pp} = -EA_p$ is Electron Affinity. The average value of $f_{pp} = -(IP_p + EA_p)/2$ is for one electron orbital. The diagonal matrix of the Fock operator with D_{pp} diagonal element is $F_{pq} = -(D_{pp}(IP_p + (2 - D_{pp}(EA_P))/2$ with the optimum value of 0.25 for $(IP_p) - (EA_P)$.

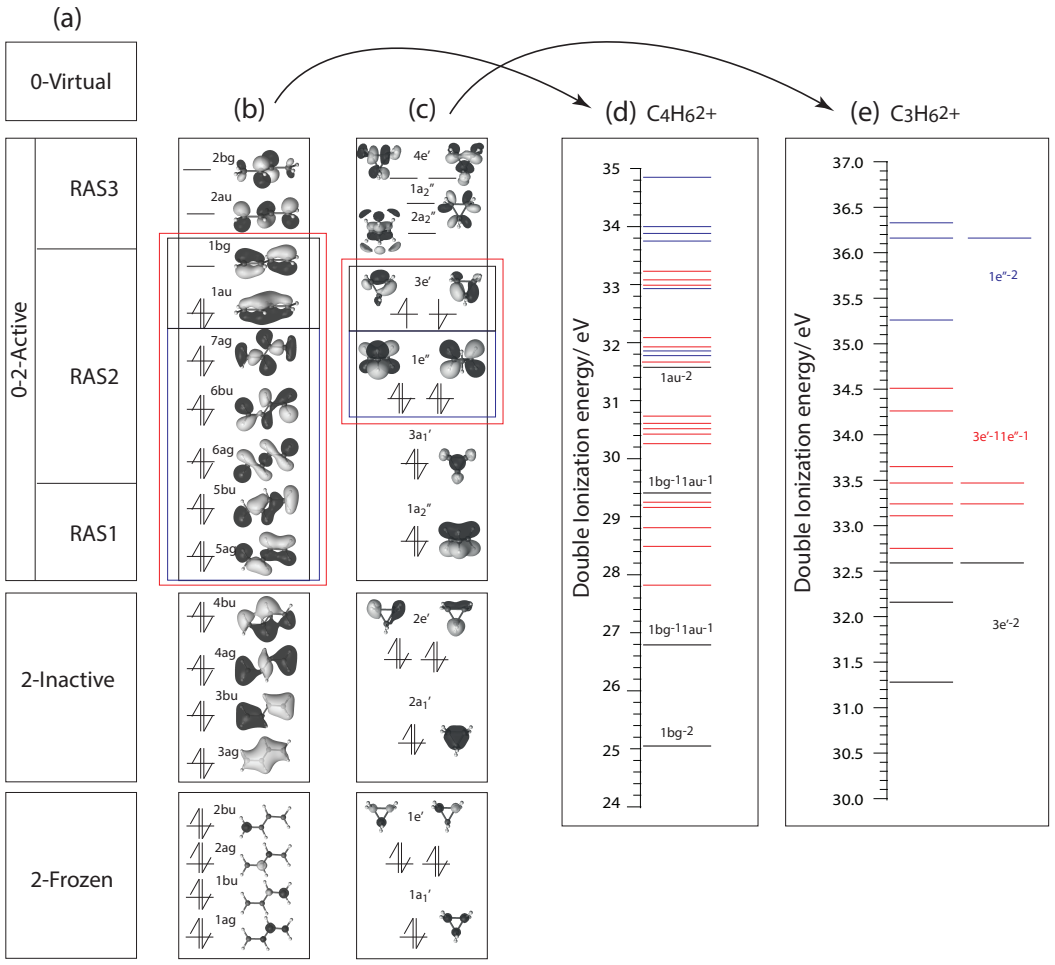

Figure 3.1: CASSCF-RASSCF orbital space including keywords and electron occupancy ranges (a). Butadiene dication states (d) obtained at the level of CASSCF-CASPT2/cc-PVTZ calculation with an active space of 12 electrons in 9 orbitals for butadiene dication (b) and cyclopropane dication states (e) obtained at the level of CASSCF-CASPT2/cc-PVTZ calculation with an active space of 10 electrons in 10 orbitals (c).

RAS2, and RAS3. Restrictions are introduced into the RASl and RAS3 subspaces such that in RASl a maximum number of holes and in RAS3 a maximum number of electrons are allowed. The remaining active electrons are distributed in all possible ways among the RAS2 orbitals, which in this case corresponds to the active orbitals in CAS type wavefunctions [see Fig. 3.1 (a)].

There are many arguments for selecting the active space [59]. For proper selection of active space chemical intuition is required. This allows us to include specific orbitals that are important in describing the chemistry relevant for our problem. In general the frontier molecular orbitals, HOMOs and LUMOs, are crucial to describe any photochemical mechanisms. For instance, in butadiene photochemistry

an obligatory choice is the four π-orbitals, and for cyclopropane dissociation an obvious choice is the highly strained σ-orbitals making C-C bonds.

Dications of butadiene and cylopropane

To interpret our experimental results, it is necessary to connect ionization dynamics to molecular structure and identify from which orbitals electrons are removed during ionization. Let's overview the calculated electronic structure of the butadiene and cyclopropane dications. Singlet and triplet electronic states of the dication are obtained using parallel CASSCF-CASPT2 calculation as implemented in the MOLCAS software program [60]. The cc-pVTZ basis set is used for these calculations. The orbitals were obtained from a CASSCF calculation with an active space of 12 electrons in 9 orbitals for butadiene, as indicated in Fig. 3.1 (b), and 10 electrons in 10 orbitals in cyclopropane, as indicated in Fig. 3.1 (c). These result in the first 27 singlet and triplet states of the butadiene dication shown in Fig. 3.1 (d), and the first 17 singlet and triplet states of the cyclopropane dication shown in Fig. 3.1 (c). From the orbital vacancies and density (degeneracey) of states one can distinguish the difference in the patterns of the excited states in these molecules. The dication states are categorized based on the type of ionized orbitals (π^{-2}, π^{-1} σ^{-1}, and σ^{-2}) [indicated in the figure by three colors]. In butadiene the diction ground state is singlet with two holes located in the π-type HOMO ($1bg^{-2}$) which is well separated from the lower energy σ-type orbitals, and by increasing the ionization energy contribution of the σ-type orbitals increases. On the contrary, in cyclopropane the dication ground state is triplet with two holes located in one of the degenerate σ-type HOMOs ($3e'$), and by increasing the ionization energy the contribution of the π-type orbitals increases.

3.2 Geometry optimization

For an excited molecule under collision-free conditions, the ratio of dissociation is determined by the unimoleculear reaction rates. The unimolecular dissociation rate is strongly influenced by the partitioning of internal energy into the 3N-6 degrees of freedom of the parent molecule. This means that a bond elongation is much more complex that a simple bond dissociation; instead the remaining 3N-7 degrees of freedom might accompany the bond elongation by nuclear rearrangements (isomerization) processes. Within the Born-Oppenheimer approximation, the geometry

of a molecule at absolute zero temperature corresponds to the minimum of the total energy,

$$(x_i, y_i, z_i)_{T=0} = argmin(< \Psi|\widehat{H}|\Psi >). \tag{3.4}$$

The process of finding the nuclear coordinates that minimize the potential energy is known as geometry optimization[6]. The zero gradient, $\partial E/\partial x_i$, is found and evaluated by the Hessian value, $\partial^2 E/\partial x_i \partial x_j$; if the gradient is zero and Hessian value is positive the nuclear geometry belongs to the maximum energy of the PES and if it is negative the nuclear geometry corresponds to the minimum energy of the PES. Fig. 3.2 shows the procedure in which we can "walk on the PES" in a controlled way to find the minimum geometry. In multi-atomic molecules the potential energy curve consists of a one-dimensional cut through the internal coordinate spaces of the molecule with 3N-6 dimensional hyper-surfaces. Exploring the energy profile of a reaction through specific internal coordinates requires geometry optimization with the restricted coordinates. The standard approach to find the restricted energy optimized geometry is to use the Lagrangian multipliers, $L(q, \lambda) = E(q) - \lambda^T R(q)$[7].

[6]In optimization, quasi-Newton methods [61] (a special case of variable metric methods) are algorithms for finding local maxima and minima of functions. Quasi-Newton methods are based on Newton's method to find the stationary point of a function, where the gradient is 0. Newton's method assumes that the function can be locally approximated as a quadratic in the region around the optimum, and uses the first and second derivatives to find the stationary point. In higher dimensions, Newton's method uses the gradient and the Hessian matrix of second derivatives of the function to be minimized. As in Newton's method, one uses a second order approximation to find the minimum of a function f(x). The Taylor series of f(x) around an iterate is $f(x_k + \Delta x) \approx f(x_k) + \nabla f(x_k)^T \Delta x + \frac{1}{2}\Delta x^T B\, \Delta x$, where ($\nabla$ f) is the gradient and B an approximation to the Hessian matrix. The gradient of this approximation (with respect to Δ x) is $\nabla f(x_k + \Delta x) \approx \nabla f(x_k) + B\, \Delta x$, and setting this gradient to zero (which is the objective of optimisation) provides the Newton step, $\Delta x = -B^{-1}\nabla f(x_k)$, where the Hessian approximation B is chosen to satisfy $\nabla f(x_k + \Delta x) = \nabla f(x_k) + B\, \Delta x$.

[7]A Taylor expansion to 2nd order of $L(q, \lambda)$ around q_0 and λ_0 gives

$$L(q_0 + \Delta q, \lambda_0 + \Delta\lambda) = E(q_0) + \Delta q^T \frac{\partial E(q_0)}{\partial q} + \frac{1}{2}\Delta q^T W \Delta q - \lambda^T R(q_0) + \frac{\partial R(q_0)}{\partial q}\Delta q, \tag{3.5}$$

where W is defined as

$$W(q, \lambda_0) = \frac{\partial^2 E(q_0)}{\partial q^2} - \Sigma_{i=1,m}(\lambda_0)_i \frac{\partial^2 (R(q_0))_i}{\partial q^2} \tag{3.6}$$

This sets up the equation for the generalized elimination method. In the subspace which fulfil the constraint any displacement Δq must be such that

$$\frac{\partial R(q_0)}{\partial q}\Delta q = 0 \tag{3.7}$$

Using the quasi-Newton condition applied to Eq. 2.3.12 we find that the effective gradient to be used in an Hessian update procedure applied only to the molecular part of the Lagrangian Hessian

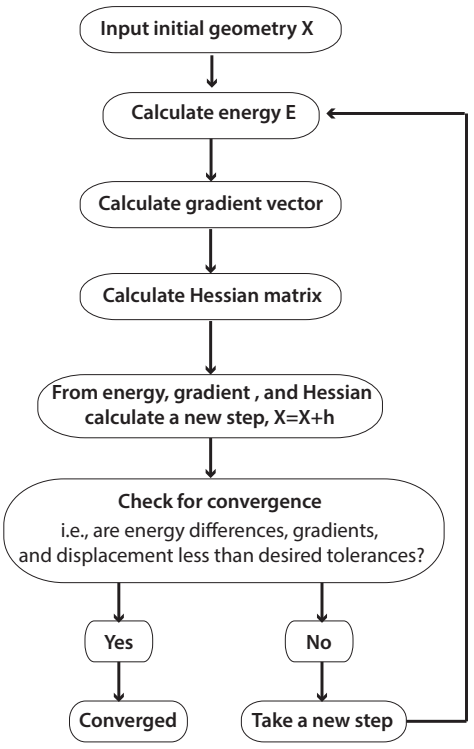

Figure 3.2: Self-consistent field (SCF) geometry optimization.

The use of appropriate coordinates is one of the best ways to improve the geometry optimization. Besides the selection of coordinates and the initial structure, the efficiency and stability of a geometry optimizer depends on the start Hessian, the update of the Hessian, and the step selection. For the update of the Hessian and the step selection accurate gradients are required. Density functional theory (DFT) is a great deal [62] for the geometry optimization. In DFT the particle density $\rho(r) = \int d^3r_2 ... \int d^3r_n \psi(r_i)\psi(r_i)^*$ is the central quantity depending on only three spatial variables ($r = (x, y, z)$), and total energy is only determined by overall electronic density E = E[$(\rho(r))$]. Verification of DFT for describing the ground state properties of large systems has been proved by Hohenberg-Kohn (HK) theorem [63]. The total energy of a n-electron system formulated by Kohn-Sham (KS),

---

is

$$H(q, \lambda) = \frac{\partial E(q)}{\partial q} - \frac{\partial R(q)}{\partial q}\lambda. \tag{3.8}$$

The procedure is started by evaluating a series of $H(q, \lambda)$ for different values of q and a fixed value of λ. A suitable value of λ is the first-order estimate of λ at convergence as given by $H(q_0, \lambda_0) = 0$.

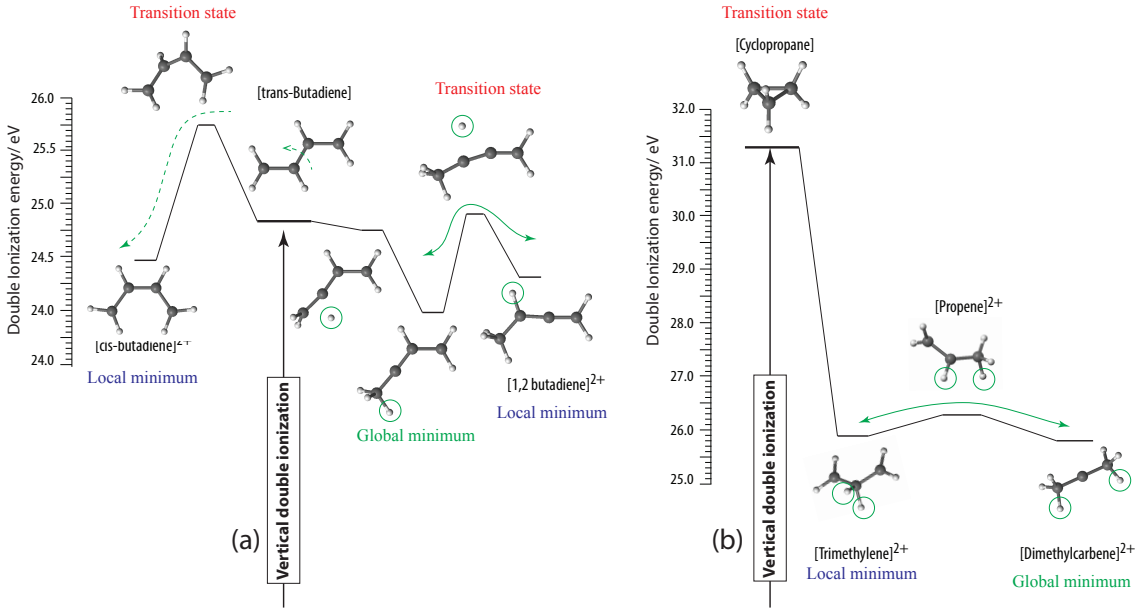

Figure 3.3: Adiabatic presentation of the PES of butadiene (a) and cyclopropane (b) dication ground state calculated at the level of B3LYP/6-31G*.

$H^{KS}\psi = E_i\psi$, is given by the KS one-electron operator

$$H_i^{KS} = -\frac{1}{2}\nabla^2 - \Sigma_I^N \frac{Z_I}{|r_i - R_I|} + \int \frac{\rho(r)}{|r - r'|}dr' + \frac{\delta E_{xc}}{\delta\rho} \tag{3.9}$$

under the constraint $< \psi_i|\psi_j >= \delta_{ij}$. Using the variational approximation of the Coulomb potential, the gradient accuracy is coupled to the self-consistent field (SCF) convergence and the accuracy of the numerical integration of the exchange-correlation potential.

Dications of butadiene and cylopropane

In Fig. 3.3 (a) and (b) adiabatic presentation of PESs of the dication ground state of butadiene and cyclopropane are shown. Both the neutral and the dication energies were optimized using B3LYP/6-31G* in order to obtain the double ionization potential. Following vertical double ionization (to the Franck-Condon region) both butadiene and cyclopropane dications are left with sufficient internal energy for nuclear rearrangement. The extent of nuclear geometry change following double ionization depends on the difference between potential energy of the dication at the FC region and at the equilibrium geometry, known as adiabatic double ionization potential. As seen in Fig. 3.3 (a), the vertical and adiabatic double ionization potential of butadiene differ by 1.5 eV, and the difference leads to convention of electrons energy

to nuclear kinetic energy, where the nuclear wave-packet is moving up and down along the PES via H-atom scrambling between different C=C bonds (H-migration). The reversible H-migration due to the delocalized π-electrons along the carbon chain is known as a characteristic of π-conjugated systems, the so-called tautomerization[8] [64]. In competition with H-migration, butadiene *trans-cis* conformation may occur if vertical double ionization leaves the dication with 1eV excess internal energy. On the contrary, as seen in Fig. 3.3 (b), the vertical and adiabatic double ionization potentials of cyclopropane differ by about 6 eV, which leads to irreversible conversion of electronic energy to nuclear kinetic energy via ring-opening. In paper I and III nuclear dynamics following double ionization of these molecules is investigated by comparison of the geometry optimization calculations and ion-ion coincidence measurements.

[8]Tautomers are isomers that differ by the location of a proton and a π bond.

Chapter 4

Experimental methods and applications

The experimental work in this thesis was conducted using a 3D-imaging multi-coincidence ion spectrometer at the Swedish national laboratory for synchrotron radiation, MAX-lab, located in Lund Sweden[65]. Experimental work in valence-ionization region (papers I-III) was performed at the high resolution normal incident beamline I3 of MAX III ring [66, 67]. In the studies involving core excitation (papers II-IV-V) the soft x-ray beamline I411 on the MAX II storage ring is used [68, 67].

4.1 Synchrotron radiation

Electromagnetic radiation is created when a charged particle is accelerated [69]. The so-called synchrotron radiation is generated when relativistic electrons are accelerated radially by bending magnets [70]. The radiation forms a narrow cone in the direction tangential to the electron trajectories spanning a broad range of photon energies with linear polarization in the plane of the orbit and elliptically out of the plane.

When a relativistic electron follows a curved path, synchrotron radiation is created and electron loses a fraction of its kinetic energy. This energy loss is compensated by boosting the electron kinetic energy in RF cavity. Figure 4.1 shows a schematic picture of a third-generation synchrotron-radiation facility, where the synchrotron radiation is provided more efficiently by an insertion device undulator. An undulator consists of a periodical structure of dipole magnets which force the electrons to undergo oscillations with period length λ_u and variable amplitude B_u via ad-

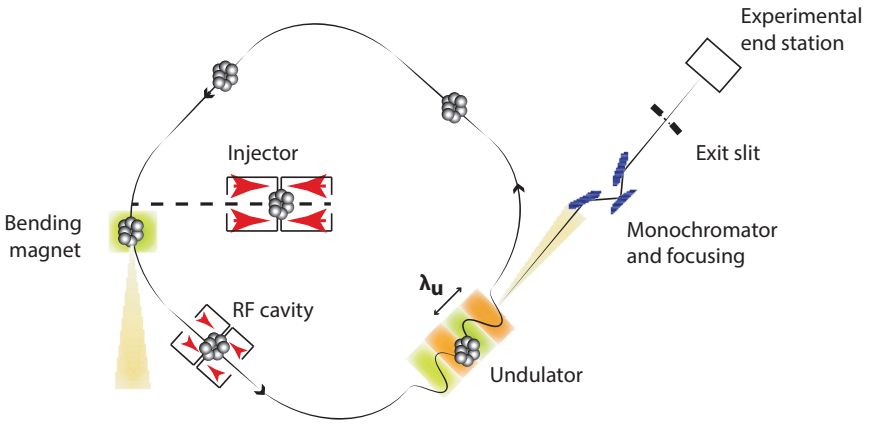

Figure 4.1: Third-generation synchrotron radiation facility. The electron bunches are injected into the ring and give the time-structure of the light with duration and separation times. The relativistic electrons are synchronized via bending magnet to pass through the RF cavity. Using undulator polarized brilliant radiation is tuned and after monochromatization focused and sent toward experimental end station.

justable gap between the magnet poles. The undulator radiation is highly collimated, has high flux and brilliance (more than 10^{18} photons/s/mm^2/mrad^2/0.1%BW), and consists of a sequence of sharp peaks. The frequency of undulator radiation at each maximum is to a good approximation given by

$$\lambda_n = n\frac{2c\gamma^2}{\lambda_0}(1 + \frac{K^2}{2} + \gamma^2\theta^2)^{-1}, n = 1, 2, 3, ... \tag{4.1}$$

$$K = \frac{eB_u\lambda_u}{2\pi m_e C_0} \tag{4.2}$$

where θ is the emission angle with respect to the undulator axis, the γ is the Lorentz factor defined by the relativistic electron energy and K is the undulator parameter. The photon energy is adjusted by changing the gap between the magnet poles, e.g. changing the B_u in the undulator.

The light is sent through a beamline with a tunable monochromator which selects the photon energy from a few to a few thousand electron-Volt. The tunability of the photon energy gives the ability to study site- and state- selectivity [8, 10, 71, 72] or scattering effects in molecules [73, 74]. The obtainable resolution is on the order of or even beyond the effect of lifetime broadening, therefore the signature of nuclear motions accompanying electronic transitions can be examined.

4.2 3D-imaging multi-coincidence technique

Many problems in molecular dynamics demand the simultaneous measurement of internal energy and particle velocity. This is provided by combination of coincident detection of particles and 3D-momentum imaging technique. The idea behind the 3D-momentum imaging technique is simultaneous measurement of all coordinates of a given particle. Here we use a technique which images transverse momentum components (P_x,P_y) on a position-sensitive detector and axial momentum P_z in time of arrival at the detector [75].

Fig. 4.2 (a) shows schematic of the 3D-momentum imaging tube used in this work. Molecules are ionized in the source region after intersection with synchrotron radiation. A strong DC electric field is applied in the source region which extracts electrons and ions that are created in an ionization event from the source point, z_0, toward the opposite direction along the z-axis (spectrometer axis). The electrons are accelerated toward a micro channel plate (MCP) detector, which detects and amplifies the electron signals by 10^6-10^8. An electron signal starts a timer for detecting ions on the other side. The ions created in the source region are extracted, then accelerated through an acceleration region (AR), and finally enter a field-free drift tube (DT). Ions flying through the DT are detected with a MCP detector combined with a delay line anode which measures both TOF and position information (x,y) of the original impact.

4.2.1 Time-of-Flight mass spectrometry

In a time-of-flight mass spectrometer such as the one we have, the mass information is contained in the arrival time of the ion to the detector [76, 75]. If all ions were formed in a plane parallel to the source electrodes with zero initial velocity the flight time would be the same for all ions which had the same mass over charge ratio, and the resolution would be limited only by the detecting equipment. In practice the mass resolution is determined by two parameters; ionization source size and initial velocity. The distribution along the spectrometer axis, ΔS, broadens the initial position of ions, z_0. Ions starting at $z<z_0$ spend more time on the source field, gain more energy from the extracting field, and arrive with a greater speed. Wiley and McLaren presented conditions for axial focusing to make the TOF independent of z [77]. In a two field regions TOF spectrometer flexible focusing condition is obtained just by adjusting the ratio between the extraction field, E_s, and acceleration region

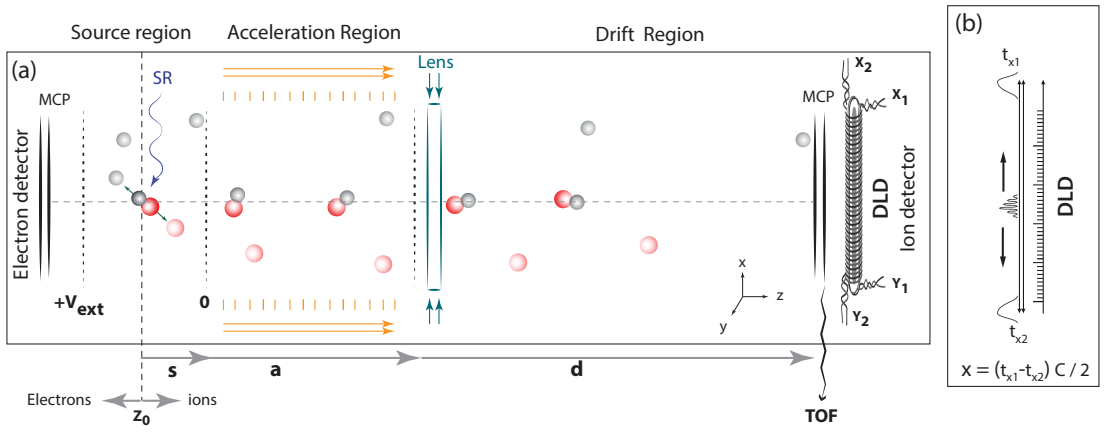

Figure 4.2: Schematic view of the 3D-ion momentum imaging tube. Molecules are ionized in the source region after interacting with synchrotron radiation. Created electrons and ions fly in opposite directions. Time window of the ion position sensitive detector [Delay Line Anode Detector (DLD)] starts with an electron signal detection. Ion trajectories are focused both axially and radially toward the DLD. The principle of position measurement is shown in (b). A signal arrives on the ion detector induces two current pulses through the two orthogonal wires. Here it is shown for the x-direction. The pulse travel to the two ends of the wire. The difference in arrival time gives the position of the first impact.

field, E_a. The total TOF through the spectrometer is determined by the flight-tubes three regions, TOF $=T_s+T_a+T_d$. To minimize the dependence on the initial location, the boundary condition $\frac{\partial TOF}{\partial z}\big|_{z=z_0} = 0$ is applied which gives the following relationship between the length of the regions and the electric fields:

$$D = 2s(k_0)^{\frac{3}{2}}\left(1 - \frac{1}{k_0+\sqrt{k_0}}\frac{d}{s}\right). \tag{4.3}$$

where k_0 is equal to the $(sE_s+dE_a)/(sE_s)$. The lengths of the regions are fixed so the ratio of the electric fields E_a/E_s is uniquely determined by Eq. 4.3. In the current spectrometer the focusing condition has been achieved numerically by the E_a/E_s ratio equal to 9.97.

To identify ions, we can use the following relation for the TOF,

$$TOF = a + b\sqrt{\frac{m}{q}} \tag{4.4}$$

where a and b are constants related to the electric fields.

Particles measured from dissociation of a molecule possess momentum due to

the kinetic energy released (KER) in dissociation. The momentum in the direction of the spectrometer axis, $\overrightarrow{P_z}$, is reflected in the TOF, and thereby affects the mass resolution. The KER in dissociation is sometimes critical for resolving heavy ions where the backward time of flight overlaps with the heavier ion. The time separation due to the backward-forward velocity is determined by the extraction field, $\Delta T = 2P_z/qE_s$, where q is charge of ions, while TOF separation of different masses is determined by the length of the DT. In order to resolve large masses a long DT is used as a dispersive element. In the current spectrometer, with a tube that is 75 cm long, for the typical energy released in dissociation, 10 eV, fragments of a few ten a.m.u can be resolved [75].

4.2.2 Momentum imaging

In imaging techniques all information about kinetic energy and angular distributions are extracted from two-dimensional image. The micro channel plate (MCP) detector combined with delay line anode records the position (x,y) of the original impact with accuracies of 25 μm. In Fig. 4.2 the position sensitive detector (PSD) is shown. Two chevron-stacks of MCPs are mounted in the xy plane, centred at the z-axis (spectrometer axis) [78]. The electron charge cloud from the MCPs is collected by a position-sensitive delay line anode detector (DLD), made by copper wires wrapped in two layers around a base plate, propagate toward the end of the wires, see Figures 4.2 (b) for a single wire, and the position (x,y) can be determined by the difference in the arrival times at the end. The TOF coordinate are taken from the MCP-back signal or with the average of the four position-signal of the DLD. The resulting (x,y,TOF) Cartesian coordinates provide the full kinematic description for a particle. Ion trajectory simulation in ref [75] shows that the radial distribution of the particle has linear dependence on perpendicular kinetic energy of the particles, $E_r = mv_R^2/2$. Thus, a complete dataset of P_z and P_r can be used to extract the kinetic energy of particles, $E_K = (P_z^2 + P_r^2)/2\mathrm{m}$.

In order to exploit the imaging method to its full potential one needs to explore methods for improvement of the spatial quality of the 2D image. The principal advantage of the current set-up is to use a simple electrostatic lens, at the beginning of the DT, which preserves the angular information and TOF focusing condition. The lens operates such that particles with the same transverse momentum components are mapped on the same point on the detector, irrespective of their initial transverse source points (x_0, y_0) from the ion lens axis [79]. The focusing capability at different

source points and KE by simulation using SimIon analysis shows that the TOF in the Wiley McLaren arrangement is unaffected by the lens focusing and transverse distribution of source region, and that axial focusing is achieved for kinetic energies from 0 to 5 eV. The lens provides radial focusing that is independent of the kinetic energy of the particles [75].

4.2.3 Coincidence

Several particles from the same event can be detected in a coincidence measurement. One of the main challenges in coincident measurement is to construct a restricted condition for the simultaneous detection of correlated fragments. False coincidences appear when the ions originating from other events are detected. To avoid false coincidences the number of ionization events, k, in the time window should be minimized. According to the Poisson distribution, $f(k) = (\lambda t)^k e^{-(\lambda t)}/k!$, the false coincidences will be diminished if $f(1) >> f(k > 1)$. This is adjusted by the count rate of the triggering electrons, λ, and the time interval, t. Practically the adjustment is done by controlling the gas flow and the photon flux.

Considering complete separation of ionization events, each dissociative photoionization event yields n-partner fragments flying far from the center of the mass, and thus kinematically obeys energy and momentum conservation. 3D-coincidence measurements of the n fragments gives 3n-3 set of (x,y, TOF). The 3n cartesian components of the fragment momentum vectors in the laboratory frame are determined by the 2n spatial coordinates, n-1 arrival time differences, and the projection of the flight times on the spectrometer (z-)axis. Our PSD is based on the timing signals, thus multi-hit fast timing electronics are complemented for coincident measurements. RoentDeK ATR-19 discriminator is used to convert the output pulses of the PSD to NIM-standard pulses [78]. The ATR-19 discriminator has 20-25 ns dead-time for detecting the second particle. In practice, two particles must be separated by at least 25 ns in order to be regarded as two separate events. This put limitations on detection of identical particles; only those with significantly different momentum can be measured in coincidence.

4.2.4 TOF vs. TOF

In dissociative double-ionization of a molecule, ejection of two electrons into the continuum is followed by charge separation into two singly-charged fragments. Due to the Coulomb repulsion a noticeable kinetic energy is released through the charge

separation step which shifts the ion's TOF. This disadvantage can, however, be turned into advantage, by formation of a tilted pattern with slope of, S= $-q_1p_{z2}/q_2p_{z1}$, on the 2D histogram of faster coincident ion vs. slower coincident ion, referred to as ion-ion correlation map, containing information regarding dissociation mechanisms.

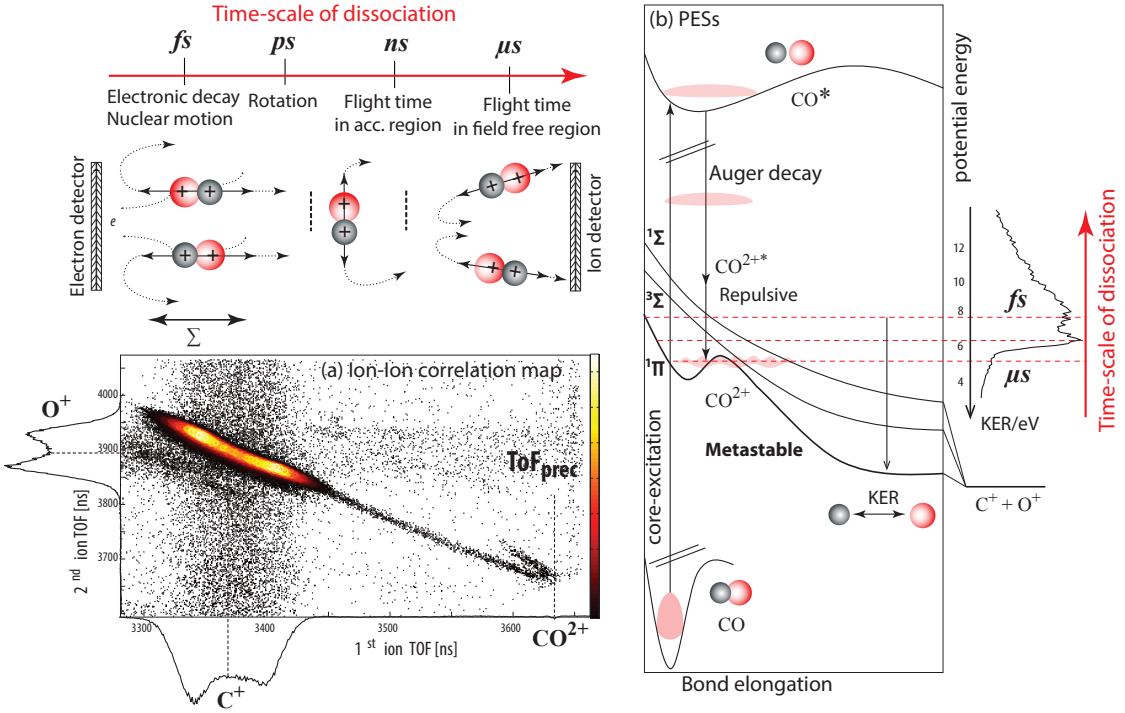

Figure 4.3: Dissociative double ionization is temporally framed by axial velocity and place of the dissociation along the spectrometer. (a). Coincident ions arising from dissociation of CO^{2+} following C1s-σ^* excitation. While the tilted pattern shows the true coincidences of C^+ and O^+, the broad vertical and horizontal features arise from false coincidences where within a time window ions of different ionization events are detected in coincidence. The extended "tail" indicates metastable dissociation in different timescales ranging from femtosecond to some microsecond. The wave packet propagation within the PESs of the core-excited and dication states (b).

Since the fragment recoil axial momentum changes by dissociation timescale, where parent molecule rotates as flying toward the ion detector, shape and length of the tilted pattern determines the dissociation timescale (precursor lifetime). For instance, Fig. 4.3 (a) shows ion-ion correlation map of CO^{2+} dissociation at different timescales. In this example, C^+/O^+ ion pairs following CO C1s-σ^* excitation are collected. As PESs shown in Fig. 4.3 (b), following C1s excitation Auger decay populates different dication final states [80], including low-lying metastable CO^{2+} ($^1\Pi$) state containing shallow "potential well". Considering dissociation of the metastable state, dissociation takes place on different timescales, ranging from femtosecond to

some microsecond, depending on the internal (vibration) energy left upon Auger decay [81, 82, 80]. The larger the internal energy of the final dication, the larger the KER of dissociation will be, and the faster the dissociation takes place. When leaving dication with sufficient internal energy, where the wavepacket rapidly passes the "potential well", dissociation occurs in a few *fs*, leading to a high-KER of dissociation and reflecting the initial molecular alignment (with respect to the spectrometer axis) on the shape of the tilted pattern (axial recoil approximation valid). Leaving dication with less amount of internal energy where the wavepacket is trapped within the "potential well" the dissociation occurs through tunnelling process. This leads to a low-KER dissociation on longer timescales. If dissociation occurs on the timescale of molecular rotation (in a few *ps*) the initial molecular alignment is lost creating a (isotropic) cigar-shaped tilted pattern, and if the lifetime of dication is long enough (*ns* timescale) to enter to the the field-free drift tube, depending upon the distance to the detector, the ion's TOF are elongated which leads to creation of a "tail" on the ion-ion correlation map. The closer the dissociation to the detector, the closer the TOF of the two different masses will be. The "tail" starts at lower right hand side of the tilted-pattern and might continue to the point where the two fragments have same TOF. This is when the dication life time is long enough (μs timescale) to reach to the detector or dissociates close to the detector, where same velocity fragments lead to positive-sloped tilted pattern. The timescale of metastable dissociation is known depending on the rate of tunnelling process, which itself depends on the mass of the species, and more importantly on the shape of the "potential well". Experimentally the dication lifetime is estimated by Monte Carlo simulation of ion's trajectory along the spectrometer axis [83]. In this thesis, μs lifetime of parent dication species are determined via the extended distribution of correlated TOFs of daughter ions.

In two-body dissociation, as the simplest case, due to momentum conservation, $p_{z1} + p_{z2}=0$, the slope of the tilted-pattern created in the ion-ion correlation map is equal to -1. In polyatomic molecules many-body processes are very common where as the parent molecule dissociates into an ion pair, neutral fragments are also ejected, and thus tilted patterns of different slopes are created on the ion-ion correlation map depending upon the mechanism of dissociation [84]. For instance, ion-ion correlation map of ammonia N1s-$4a_1$ excitation is shown in Fig. 4.4 covering three tilted patterns corresponding to H^+/ NH_x^+ dissociation channels, where x ranges from 2 to 0 corresponding to two, three, and four body dissociation. The

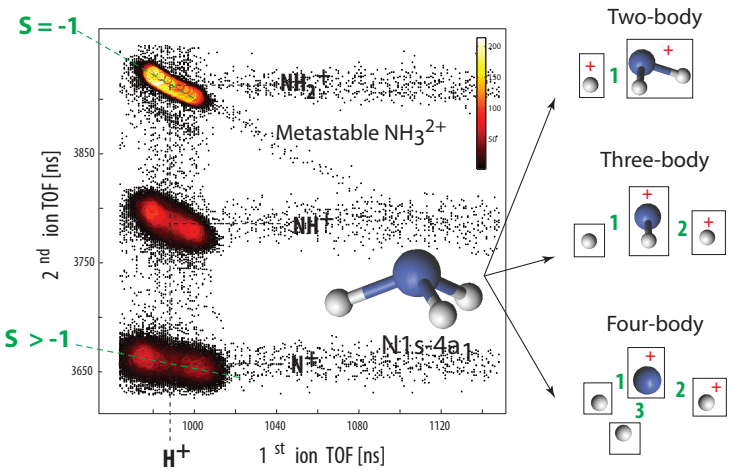

Figure 4.4: Ion-ion correlation map of ammonia N1s-4a$_1$ excitation. The three tilted pattern correspond to two, three, and four body dissociation.

metastable two-body dissociation into H^+/NH_2^+ ion pair [see the "tail"] evidences dissociation on the low-lying NH_3^{++} dication states, while the broad features of the three and four-body dissociation channels ($H/H^+/NH^+$ and $H/H/H^+/N^+$) indicates population of high-lying final states in which excess amount of internal energy releases through neutral H-ejection [85]. In four-body dissociation channel the slope $>$ -1 (-14/15) indicates that the dissociation predominantly takes place in two steps after a neutral H ejection, where the charge separation in NH_2^{2+} occurs before the second H ejection. Sequence of bond dissociation is indicated by numbers in the figure.

4.2.5 Fragment's KER correlation

In general, three-body processes upon double ionization can be divided into two mechanisms: sequential dissociation, where commonly a neutral fragment is released before the charge separation, $M^{2+} \rightarrow m_1 + M_2^{2+} \rightarrow m_2^+ + m_3^+$, and concentrated dissociation, where the neutral fragment is ejected simultaneously with the charge separation, $M^{2+} \rightarrow m_1 + m_2^+ + m_3^+$. To disentangle sequential and concerted dissociation mechanisms fragment's kinetic energy correlation is presented within the Dalitz plot [86, 87]. In this method, for each event squared momentum, $\epsilon_i = |P_i|^2/\Sigma_j|P_j|^2$, is used and due to the normalization to $\Sigma_i\epsilon_i = 1$ the coordinates extend through the two dimensions of $[(\epsilon_3)/(E_k\text{- }1/3)]$ and $[(\epsilon_2\text{-}\epsilon_1)/(E_k\ \sqrt{3})]$, where E_k is the total kinetic energy released in dissociation. Momentum conservation requires the data points in the Dalitz plot to lie inside a circle with radius 1/3, centred at the origin, as shown in Fig. 4.5 (a). Presenting fragment's kinetic energy correlation within the Dalitz plot, preferred dissociation mechanisms can immediately be recognized from

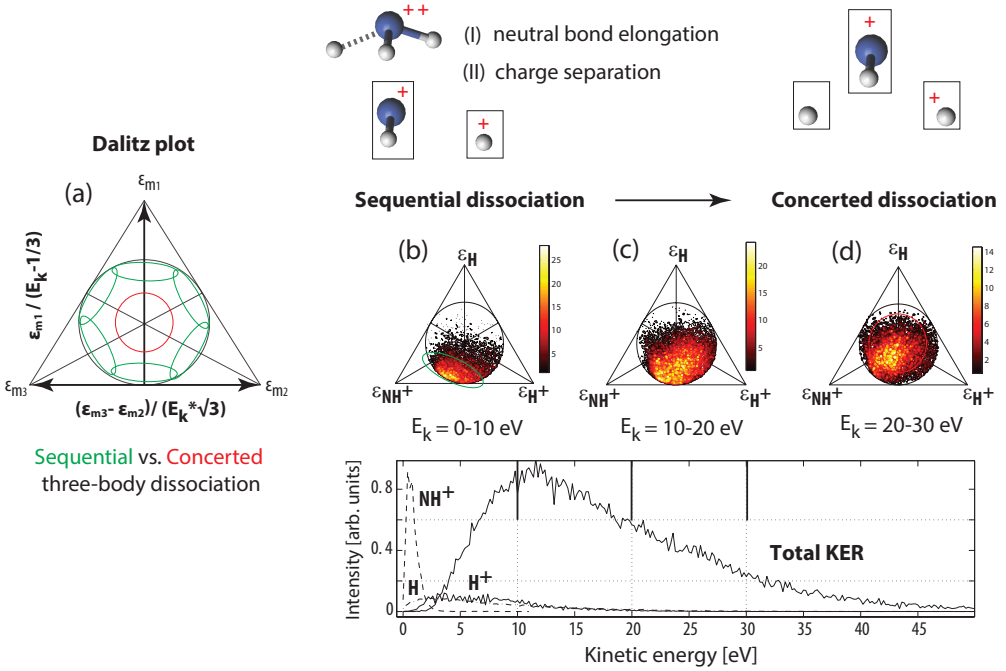

Figure 4.5: Intensity distribution within the squared momentum coordinates of Dalitz plot of three-body dissociation differs for sequential and concerted mechanisms (a). Mechanisms involved in the three-body dissociation following ammonia N1s-4a$_1$ excitation is studied using KER-filtered Dalitz plots. Sequential dissociation (b) changes to concerted dissociation (d) from low KER range to high KER range.

the intensity distribution of features.

For instance, in Fig. 4.5 mechanisms of three-body dissociation into H/H$^+$/NH$^+$ in ammonia N1s-4a$_1$ excitation is investigated within the total KER-filtered Dalitz plots. Different regions of the Dalitz plots is dominated for different kinetic energy ranges. Clearly, different dissociation mechanisms are associated with these, as both sequential and concerted processes are identified in the data. The features observed for 0–10 eV KER [see Fig. 4.5 (b)] shows low intensity distribution perpendicular to the H axis and the NH$^+$ and the H$^+$ fragments are anti-correlated to each other, which is an indication of a sequential dissociation, in which neutral H is ejected in the first step. This could be attributed to the ultra-fast N-H bond elongation upon N1s-4a$_1$ excitation, where loss of the neutral H occurs prior to Auger decay imparting a relatively low KER to the neutral H [88]. The features observed for 10–20 eV KER [see Fig. 4.5 (b)] shows evidences of both sequential and concerted dissociation mechanisms. Whilst asymmetrical distribution appears on the NH$^+$ axis reflects that the H and H$^+$ are emitted with equal momenta during a concerted

breakup, evidence of sequential dissociation is still seen as the NH^+ fragment carries away more significant kinetic energy. For the higher KER range, 20-30 eV KER [see Fig. 4.5 (c)] the asymmetrical distribution is more shifted to the center implies processes with a much more concerted character than those taking place in lower KER ranges.

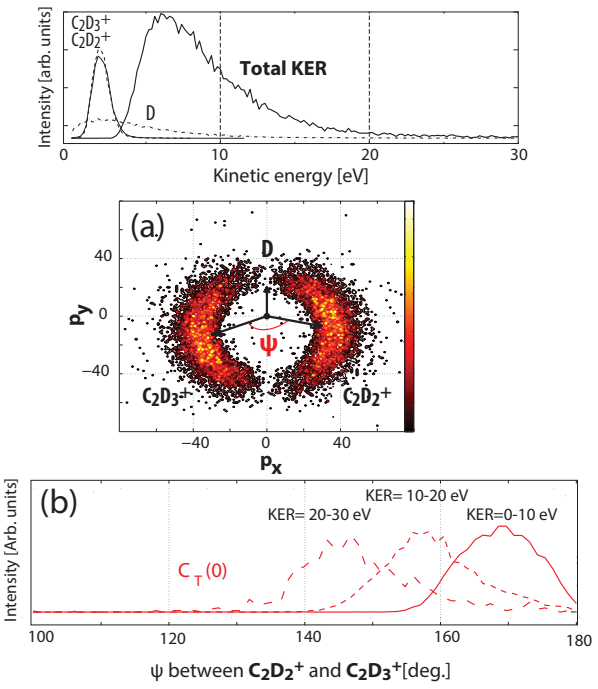

Figure 4.6: Newton plot of a three-body dissociation channel in fully deuteriated butadiene following C1s-π^* excitation. The KER-filtered histogram of angles between ionic fragments in the three-body dissociation of the fully deuteriated (b).

4.2.6 Fragment's angular correlation

Fragment's momentum correlation can be presented in different ways beyond determining the total KER of three-body dissociation. In Dalitz plot fragment's KER correlation are presented in such a way that conserves both temporal and structural information; however, for direct visualization of the molecular structure at the instant of dissociation, presentation of fragments angular correlation is required. This is possible within the Newton plot [89, 90], in which relative distribution of fragment's momentum around the center of the mass of the fragments (the position of the parent molecule) is shown on the 2D plane of momentum conservation. In the laboratory frame the common plane of the three fragments' momenta is arbitrarily oriented in space because we detect events for all molecular orientations. During data analysis we rotate the three momentum vectors of each event such that they have only non-zero components in the (x,y) plane. An example of Newton plot is shown in Fig. 4.6 (a) for a three-body ($D/C_2D_2^+/C_2D_3^+$) dissociation channel in

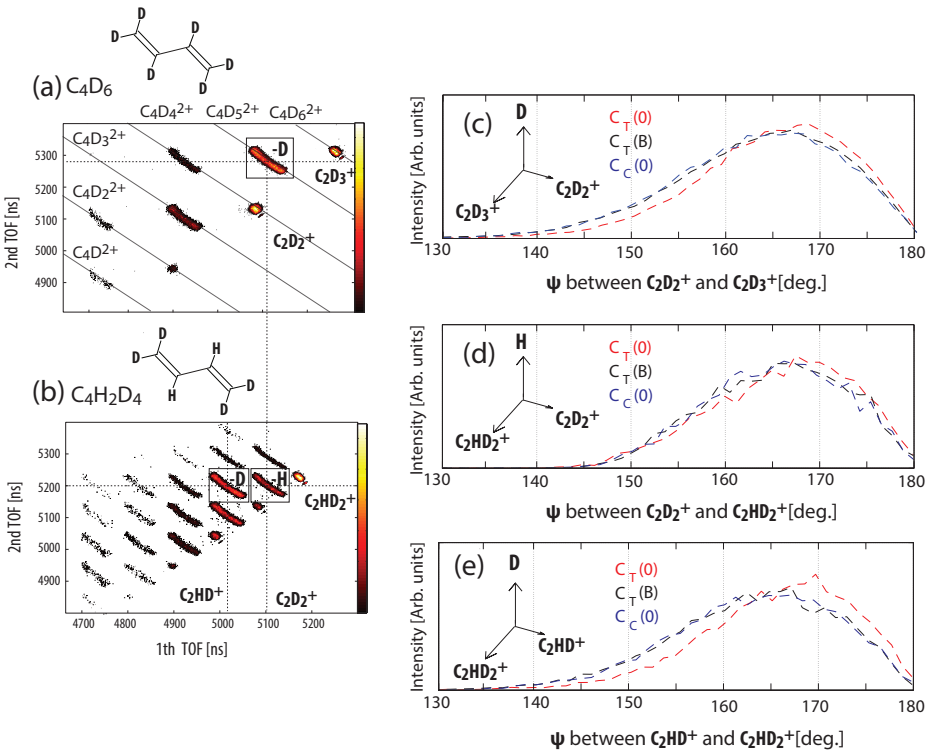

Figure 4.7: The ion-ion correlation map upon C1s-π^* excitation in fully (a) and partly (b) deuteriated samples. The histogram of the angles between two ionic fragments in the three-body dissociation channels of the fully deuteriated (c) and the partly deuteriated (d) and (e) samples for different C1s resonance excitations.

butadiene (C_4D_6) upon C_T1s to π^* excitation. The fragment's vectors are rotated such that the deuterium has only a non-zero component in the y direction, which is always positive. This means that the deuterium is always directed vertically, but its momentum is not drawn. Instead, we plot the momentum distributions of the two heavy fragments in the common (x,y) plane where the x momentum components of the $C_2D_2^+$ ions are restricted to positive values and those of the $C_2D_3^+$ ions to negative values. The momenta of the $C_2D_2^+$ and the $C_2D_3^+$ ions form a ring-like structure with an off-set center from the origin in y-direction reflecting the recoil of the deuterium momentum, which indicates well a two-step sequential dissociation where D is ejected prior to charge separation. As a basic rule in dissociation of hydrocarbons, ejection of light mass of H atoms acts as a "cooling" process to prevent dissociation of the carbon chain. This means that following Auger decay populating final states the molecule ejects several H atoms depending on the internal energy. As seen in the ion-ion correlation map of deuteriated butadiene (C_4D_6) upon C_T1s to π^* excitation

covering charge separation through the central C-C bond dissociation [see Fig. 4.7 (a)] several ion pairs appear in which the total number of D atoms differ. Considering three-body dissociation in the planar geometry, where one D atom is ejected prior to charge separation into $C_2D_2^+/C_2D_3^+$ ion pair (D), the more the internal energy is released via the D-ejection, or to the lesser extent the D-ejection occurs out of the molecular plane, the smaller the angles between two ionic fragments will be. As seen in Fig. 4.6 (b), the role of internal energy is well reflected on the KER-filtered histogram of the angles between two ionic fragments: the angles between two ionic fragments in 0-10 eV KER of dissociation range reaches larger values by about 12° degree compared to the angles in 10-20 eV KER of dissociation, and by about 24° degree compared to the angles in 20-30 eV KER of dissociation. The linear decrease of the angle with KER indicates complete transfer of excess internal energy to the KE of D-atom. While these angles are KER-dependent, the KER-independent histogram of angles between ionic fragments in the two mass-distinguished three-body channels of partly deuteriated butadiene sample ($C_4H_2D_4$) [see the ion-ion correlation map in Fig. 4.7 (b)] show that an out-of-plane nuclear motion following C_T resonance excitation precedes D-ejection. The larger angles are achieved at this photon energy compared to the vibrational excitation and central resonance excitation [see Fig. 4.7 (e)], indicating contribution of different nuclear geometries to the dissociation when the photon energy is changed over C1s excitation. This will be further discussed in section 5.2.2.

Chapter 5

Molecular photo-dissociation

5.1 Dissociative double ionization

Understanding ultra-fast molecular photo-dissociation requires deep insight into the underlying connection between electronic and nuclear motions. Provided that electronic motion sets in much faster than nuclear motion (the Born-Oppenheimer approximation), the question is to what extent and by which mechanisms electronic processes can dynamically influence or determine the outcome of molecular dissociation. This can be achieved by combining tunable synchrotron radiation and coincident ion measurements: while tuning the photon energy to (directly or indirectly) prepare doubly-ionized molecules in specific electronic states, a complete picture of dissociation is obtained when ion-ion momentum correlations are measured. By extracting the coincident data into ion-ion correlation map we identify dissociation channels, appearance energy (AE), yield of dissociation, and KER values. In what follows, one can compare the photon-dependent results with *ab-initio* multi-configurational calculations to correlate electronic and nuclear dynamics of the dissociation.

5.1.1 Coulomb repulsion vs. H-migration in butadiene (Paper I)

In dissociation of doubly charged molecules, one might think that the dominant scenario is charge separation via breaking the weakest bond. However, ion-ion coincidence measurements in a variety of molecules show that double ionization causes molecular dissociation into channels which are not expected to originate based on the bond strenght [91, 92, 93]. When a molecule becomes ionized (or excited), it

receives additional internal (electronic + vibration) energy which can lead to isomerization (nuclear rearrangement) of the parent molecule. Of all the isomerizations of hydrocarbons, only those of unsaturated ones allow a clear formulation [94]. In unsaturated hydrocarbons rapid H atom (or π-electron) replacement between adjacent and aligned C2p orbitals enables dissociation of different isomers [95, 96]. In the case of double ionization, due to the Coulomb repulsion, H-migration is, however, affected by enhancing the distance between two moving charges. At first glance in the ion-ion correlation map of butadiene (as the simplest π-conjugated system) measured at 32 eV photon energy (see Fig. 5.1), it appears that simple charge separation is overshadowed by H-migration processes: despite the fact that the central C-C bond is the weakest bond in the neutral molecule, asymmetric charge separation occurs before the symmetric one. In addition, as seen in the ion-ion map, two metastable $C_4H_6^{2+}$ and $C_4H_4^{2+}$ dication species [see the extended "tail"] are created in which H migration processes lead to asymmetric charge separation and CH_3^+ fragments.

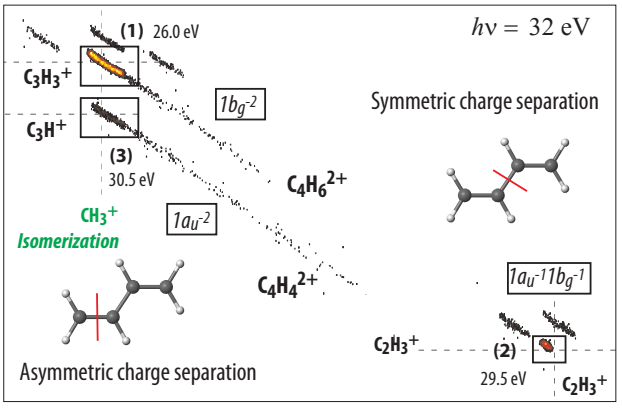

Figure 5.1: Ion-ion correlation map of butadiene at 32 eV photon energy. Symmetric and asymmetric charge separation and AE of the first three channels are indicated. In symmetric charge separation a significant fraction of the ion pairs are not measured due to electronics dead-time limitations for particles arriving simultaneously.

Comparison of the experimental results with the *ab-initio* calculated minimum energy reaction pathways shown in Fig. 5.2 indicates that, in fact, the π^{-2} states work as gateway to these dissociation channels. Double ionization of the two π-symmetric MO's, $1b_g$ making terminal C=C bonds and $1a_u$ making central C=C bond, leads to three configurations of $1b_g^{-2}$, $1b_g^{-1}1a_u^{-1}$, and $1a_u^{-2}$, in which ionization energy increases with Coulomb repulsion (distance) of the two charges along the carbon chain. As seen in Fig. 5.2, the first asymmetric charge separation, channel (1), appears at 26.0 eV, about 1 eV above the dication ground state ($1b_g^{-2}$). Calculation shows that the ($1b_g^{-2}$) state is stable with respect to symmetric charge separation, while it has sufficient internal energy for a series of sequential 1,2 H-migration. The lowest potential barrier for asymmetric charge separation is calculated to be 25.91 eV, which corresponds to charge separation in the 1,2-butadiene dication into the

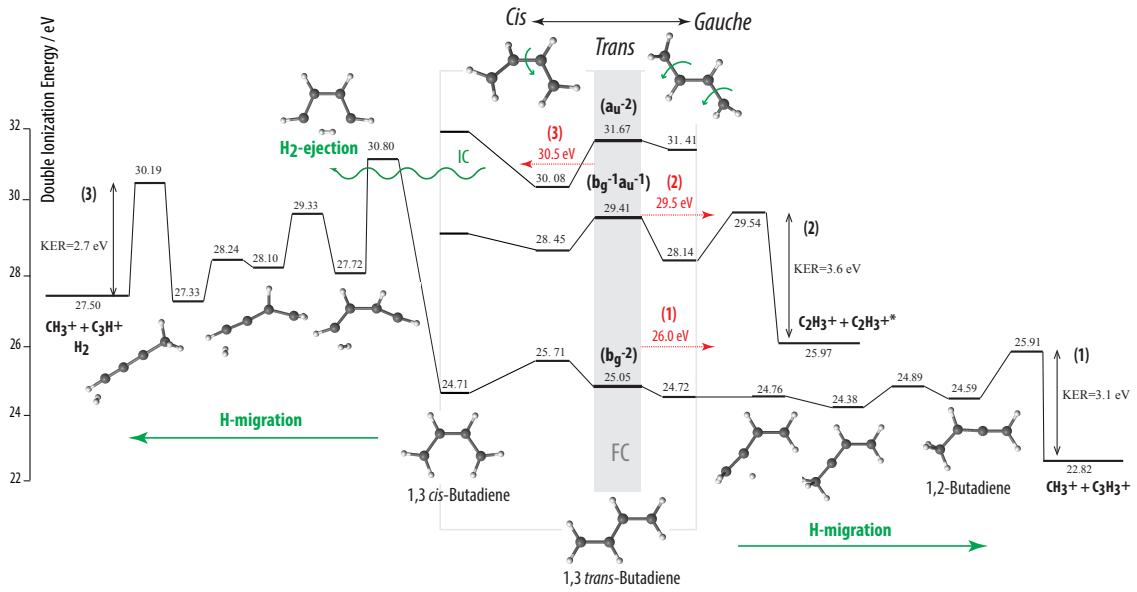

Figure 5.2: Calculated energy diagram at the level of CASCF/CASPT2-cc-pVTZ showing reaction pathways of the butadiene dication states from the Franck-Condon region to the dissociation channels (1), (2), and (3). The conformational rearrangement determines the dissociation pathways. Ion pairs in channel (1) are produced after H-migration from a central carbon to its closest terminal carbon initiated by the CH_2 twisting (*gauche*-conformer) after $b_g^{-1}b_g^{-1}$ double-ionization. H_2 evaporation takes place on *cis*-conformer through central C-C bond torsional motion.

$CH_3^+/C_3H_3^+$ cation pair [channel (1)]. Below this potential barrier a sea of $C_4H_6^{2+}$ isomers exist which are stable up to 0.86 eV above the $1b_g^{-2}$ state. This explains the creation of metastable $C_4H_6^{2+}$, and the extended "tail" seen in this channel. The direct symmetric charge separation, channel (2), appears at 29.5 eV, close to the calculated potential barrier of dissociation of the excited dication state ($1b_g^{-1}1a_u^{-1}$) at 29.54 eV energy. The second asymmetric charge separation, channel (3), appears at 30.50 eV, corresponding to the *trans* to *cis* conformation of $1a_u^{-2}$ state. The minimum reaction pathway of this channel leads to H_2-ejection from the *cis*-conformer when the two terminal H-atoms approach each other. The potential barrier of H_2-ejection from this state is calculated to lie above 32 eV. Thus, H_2-ejection from the excited states requires internal conversion (IC) to the vibrational states of the ground state. Since the IC rate depends directly on the density of vibrational states, on the order of 10^{-14} second, this provides an additional explanation for the extended "tail" that is seen for this channel. The resulting [CH-CH-CH-CH^{2+}] intermediate state has sufficient internal energy for a series of H-migration and asymmetric charge separation processes. The lowest barrier for charge separation into the CH_3^+ and C_3H^+

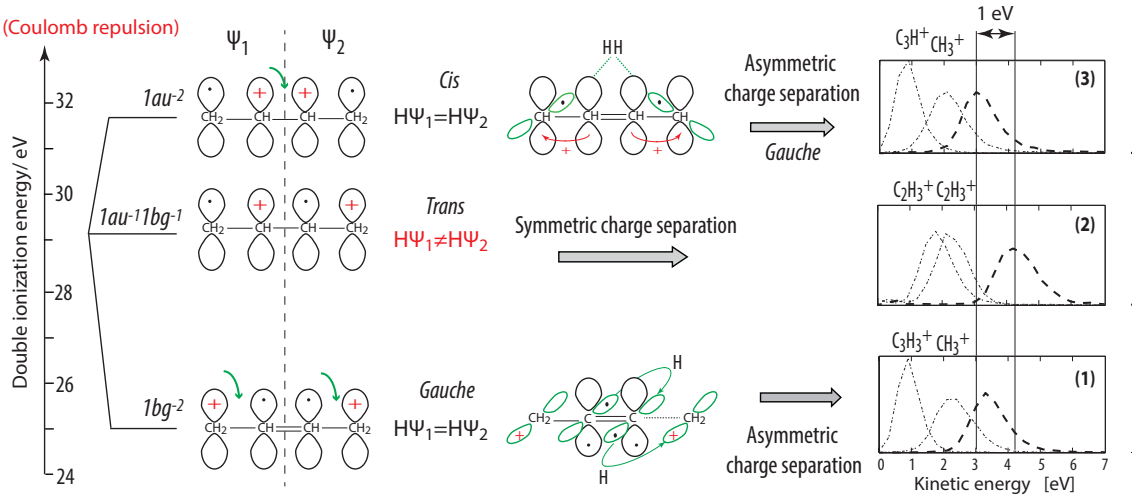

Figure 5.3: Charge separation vs. H-migration in butadiene π^{-2} dication states. Double ionization of π orbitals leads to three electronic configurations, in which ionization energy increases with Coulomb repulsion (distance) of the two charges in π orbitals. Whether the dication is stable or not is, however, determined by symmetric hole/charge distribution.

cation pair (3) is calculated to be 30.19 eV in the [CH-C-C-CH_3^{2+}] isomer, which is close to the experimental AE at 30.50 eV.

The mechanisms of dissociation following double ionization of π orbitals is schematically summarized in Fig. 5.3. Although double ionization of $1a_u$ orbital, which is predominantly distributed on the central C-C bond, leads to the highest Coulomb repulsion between the two central carbons, symmetric charge separation via central C-C bond breaking is associated to the $1b_g^{-1}1a_u^{-1}$ dication state, where the two constituent ethylene groups are symmetrically inequivalent; while double ionization to $1b_g^{-2}$ and $1a_u^{-2}$ dication states, where the two ethylene groups remain equivalent, leaves the dication stable for conformational rearrangement and charge transfer processes via H-migration and H_2-ejection. On the right side of Fig. 5.3 mechanisms of charge transfer are shown. After double-ionization of $1b_g$ orbital, the two ionized C_{2p_z}s at the end of the carbon chain are free to rotate to lie parallel to the adjacent C-H bonds attached to the central carbons (*gauche* conformation). This initiates H-migration processes from one end to another end leading to asymmetric charge separation. In double ionization of the $1a_u$ orbital, the two ionized C_{2p_z}s at the central carbons are free to rotate leading to a *trans-cis* conformation. This provides molecular hydrogen ejection from the two end carbons, moving close to each other in the *cis* conformation, which triggers hole/charge transfer processes from the central carbons to the end of the chain. A similar situation is found in the *gauche* confor-

mation which leads to asymmetric charge separation. The experimental KER of the dissociation channels shown in Fig. 5.3 are in good agreement with the calculated ones indicated in Fig. 5.2: the KER of symmetric charge separation channel reaches larger values by approximately 1 eV compared to the asymmetric charge separation channels, which confirms the significance of Coulomb repulsion in symmetric charge separation channel and charge transfer processes in asymmetric charge separation channels stabilizing $C_4H_6^{2+}$ and $C_4H_4^{2+}$ species. Therefore, we can hypothesize that in double ionization of conjugated π orbitals symmetric charge distribution leads to stable dication species and out of plane twisting/torsion motions provide a means for controlling charge transfer processes. This should be reproduced in larger π-conjugated systems.

5.1.2 Double ionization (direct or indirect)

One photon double ionization process itself provides insight into electron correlation effects. Ejection of two electrons by single-photon absorption could be classified into two mechanisms: (1) sequential (indirect) double ionization in which two electrons are removed independently, where initial ionization of an inner-valence leads to autoionization, and (2) non-sequential (direct) double ionization during which the sudden removal of one electron causes a quiver motion of the remaining correlated-electrons that "shakes" a second electron off (or knocks it out), as shown schematically in Fig. 2.2 (b). Although in the latter mechanism, due to the simultaneous involvement of two electrons and the electron-electron correlation effects, the situation of the polarized light absorption probability is complicated, and to precisely define double ionization mechanisms energy-resolved measurements of both emitted electrons is required; the study of coincident photo-ion angular distribution as a function of photon energy allows us to investigate dynamics of double ionization including the subsequent nuclear motion [97, 98].

In paper I, anisotropic angular distribution of the fragments upon dissociative double photoionization of butadiene at 35 to 45 eV photon energy is reported. The anisotropy of the angular distribution can be regarded as the combined effects of two main conditions: (a) the absorption of the VUV photon occurs when the molecule has the most favourable alignment of the orbitals involved in the double photoionization; (b) the whole double photoionization process, followed by the separation of two ionic fragments, must occur in a time frame shorter than the rotational period of the dication. Therefore, at those energies where the product ions exhibit an angular

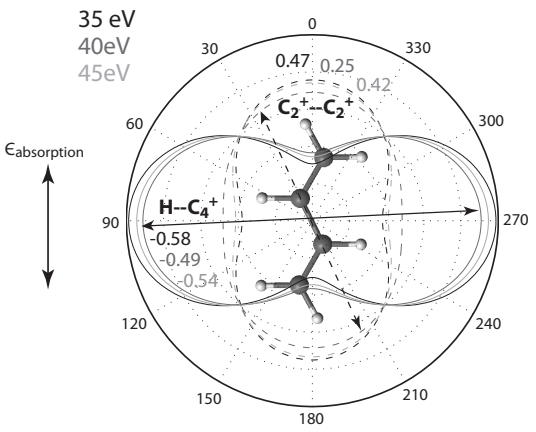

Figure 5.4: Angular distribution for β values of butadiene dissociation into $H/C_2H_2^+/C_2H_3^+$ at 35, 40, and 45 eV photon energies.

anisotropy, the two above conditions have to be completely fulfilled. In Fig. 5.4 angular anisotropy of the ejected H and carbon-based fragments in the sequential three-body dissociation $H/C_2H_2^+/C_2H_3^+$ are shown at three photon energies. Since in planar 1,3-*trans* butadiene the C-H and C-C bonds are nearly perpendicular, H-atom ejection is expected to be at very different angles with respect to dissociation of carbon-carbon bonds. At 35 eV photon energy, the measured angular distribution of the ejected H-atom is characterized by β equal to -0.6±0.1, while the angular distribution of the carbon based fragments arose after charge separation by the central carbon bond dissociation is more parallel to the polarization vector of the light with β=0.47. The well defined angular distributions indicates that both C-H and C-C bonds dissociate at time frames significantly shorter than the rotational period of the parent molecule. The molecular alignment with the carbon backbone parallel to the light polarization vector indicates the dominant parallel transition symmetry of double-ionization at this photon energy. The fact that molecular alignment at different photon energies does not show any change in the angular distributions shows no evidence of indirect double ionization through resonant excitation that populates doubly ionized states in this energy region, since β is constant with photon energy. Domination of direct double-ionization in this energy region pinpoints an important property of butadiene, that there is a strong correlation between electrons contributing to C-H and C=C bonds.

5.1.3 Selective ring-deformation in cyclopropane (Paper III)

In the field of controlling molecular dissociation cyclopropane can be regarded as an ideal example. As discussed in section 2.2.1, due to the highly strained triangular

carbon structure in cyclopropane ultra-fast ring-opening occurs at the instant of ionization of the doubly-degenerate $3e''$ orbitals (contributing to the C-C bonds), the Jahn-Teller distortion. Regarding double ionization process of 3e′ orbitals, if ultra-fast ring-opening intervenes between two electronic transitions, it enhances the possibility of indirect double ionization below the vertical double-ionization threshold [99, 100, 101]. Potential energy of the seventeen lowest cyclopropane dication states is calculated shown in Fig. 3.1 (e). The first four dication states lying in the 31.28-32.59 eV energy region correspond to double ionization of the doubly-degenerate $3e'$ orbitals. However, geometry optimization calculation indicates that the vertical double ionization leaves the the dication with sufficient internal energy for ring-opening, H-migration, and H_2-ejection [see Fig. 3.3 (b)]. We measured coincident ions when tuning the photon energy from 25 eV corresponding to the minima points (trimethylene and diethylecarbene) of dication ground state to 35 eV corresponding to population of $1e''^{-2}$ dication states. In Fig. 5.5 the ion-ion correlation map together with TOF mass spectrum covering the $C_3H_{6-n}^{2+}$ $(i = 1 - 4)$ dication species are shown. The AE of different channels are indicated in the figure. Although above the DIP_V at 31.28 eV, evidence of direct charge separation is seen: the $CH_2^+/C_2H_4^+$ ion pair appears at 31.5 eV corresponding to simultaneous dissociation of two C-C bonds, and the $H_3^+/C_3H_3^+$ ion pair appears at 32.5 eV corresponding to simultaneous dissociation of three C-H bonds; the most intensive dissociation channels occur below the vertical double ionization: the $CH_3^+/C_2H_3^+$ ion pair associated with H-migration appears at 29.5 eV photon energy, and (not the parent dication but instead) a sharp peak at m/z=20 corresponding to the $C_3H_4^{2+}$ dication appears on the mass spectrum at 30.5 eV, which later at 32.5 eV fragments into the $H^+/C_3H_3^+$ ion pair [see the extended "metastable tail" of the $H^+/C_3H_3^+$ ion pair in Fig. 5.5].

Considering two dissociation channels that lead to $CH_3^+/C_2H_3^+$ and $CH_2^+/C_2H_4^+$ ion pairs, although both channels involve breaking two C-C bonds, the ring-deformation mechanisms underlying these channels are different: two unequally elongated C-C bonds favour H-migration below the DIP_V, while two equally elongated C-C bonds favour direct charge separation. The calculated minimum reaction pathways for the $CH_3^+/C_2H_3^+$ and $CH_2^+/C_2H_4^+$ ion pairs shown in Fig. 5.6 correlates these channels to double ionization of the $3e'$ orbitals. Double ionization of the doubly degenerate $3e'$ orbitals leads to different configurations owing different bonding characteristics: while double ionization of both $3e'$ orbitals to the lowest triplet and singlet *uu/ud*

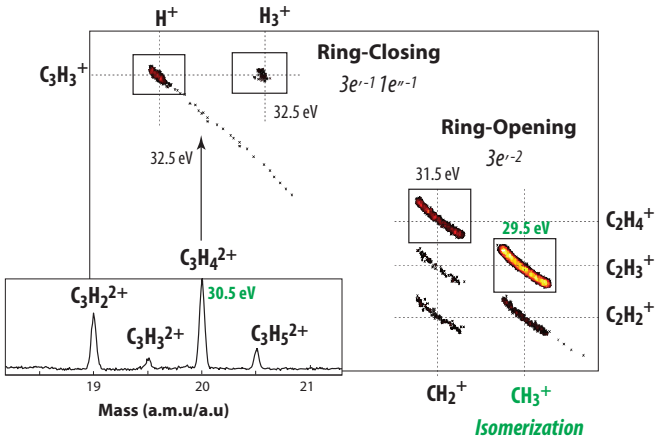

Figure 5.5: Ion-ion correlation map of cyclopropane and mass-spectrum covering dication species at 35 eV photon energy.

states symmetrically distributes two charges over the triangular carbon structure. Double ionization from one $3e'$ orbital to the orbitally-degenerate *20/02* states asymmetrically distributes the two charges over the triangular carbon structure. Accordingly, ring-deformation in these states proceeds differently: Double ionization to the *uu/ud* states spontaneously relaxes via two C-C bonds elongation, and double ionization to the orbitally-degenerate *20/02* states undergoes Jahn-Teller distortion which is predominantly along one elongated C-C bond. Equal elongation of two C-C bonds correlates the *uu/ud* dication states to the ground state of the $CH_2^+/C_2H_4^+$ ion pair; while elongation of single C-C bond creates the lower Jahn-Teller component of the *20/02* states at 25.04 eV, 6 eV below the vertical double ionization threshold, in which ionized C2p of the terminal carbons are aligned to the central H atoms (similar to the π-conjugated state) and causes the molecule to undergo H-migration (from central to terminal) or H_2-ejection (from the central carbon). The $CH_3^+/C_2H_3^+$ ion pair appears at 29.5 eV which is about 2 eV above the calculated minimum potential barrier of dissociation of the propene dication. The experimental KER of dissociation peaks in good agreement with the calculated KER of dissociation of propene dication [see Fig. 5.6 (a)]. This suggests that population of the lower Jahn-Teller component occurs through indirect double ionization processes. The intermediate highly excited singly-ionized states populated at 29.5 eV decay through autoionization and ring-opening thus populating the lower Jahn-Teller component of the *20/02* states. The $CH_2^+/C_2H_4^+$ ion pair appears at 31.5 eV, corresponding to the vertical double ionization to the *uu/ud* dication states, however the experimental KER distribution is peaked at 5 eV which is 1.5 eV less than the calculated KER of dissociation upon direct ionization [see Fig. 5.6 (b)]. This indicates domination of indirect double ionization at 31.5 eV, in which 1.5 eV internal energy is released

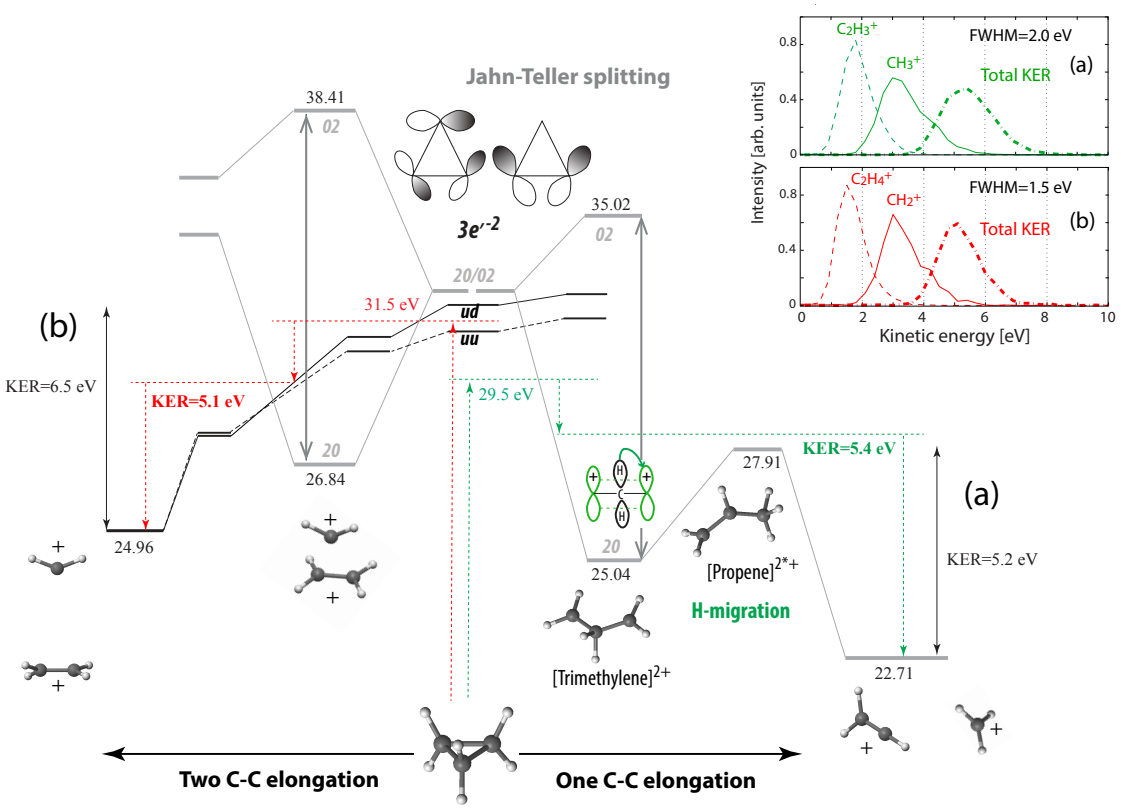

Figure 5.6: The minimum reaction pathways of dissociation following 3e′ double ionization is calculated at the level of CASSCF/CASPT2 and cc-pVTZ theory inducing cyclopropane Jahn-Teller active ring-opening. The KERD of the dissociation into $CH_3^+/C_2H_3^+$ (a) and $CH_2^+/C_2H_4^+$ (b) ion pairs indicate that an excess amount of internal energy is not involved in the dissociation channels.

through autoionization and ring-opening to the repulsive *uu/ud* dication ground states crossing with the lower Jahn-teller component of *20/02* states.

5.2 Dissociation following core-electron excitation

As discussed earlier, when a core-electron is excited in a molecule, due to the sudden change in the nuclear charge at the site of excitation, a non-stationary state is created in which the molecule starts to relax via geometry change and Auger decay. The nuclear and electronic correlations lead to population of singly and doubly ionized states, in which the molecule dissociates toward different pathways. One way to disentangle these correlations, and the role of nuclear geometry change on Auger decay is by recording dissociation dynamics while manipulating the initial condition of the wave-packet. For this propose we tune the photon energy for vibrational- site-

or state-selective core-electron excitation in molecules. For instance, in the following we investigate how dissociation pathways change upon site-selective terminal and central carbon 1s excitation in butadiene, and whether the dissociation pattern changing upon cyclopropane carbon 1s excitation to different valence orbitals (π^* and σ^*) is connected to the anti-bonding character of the valence orbitals.

5.2.1 Core-hole scattering

In principle, following core-electron excitation the nuclear geometry changes until the core-hole decays. Auger decay thus serves as a stopwatch for the nuclear motion on the femtosecond core-hole lifetime. We start our study by manipulating wave-packet propagation within the core-hole lifetime. To this end a narrow bandwidth photon energy is frequency tuned to excite a subset of vibrational states of PES. The basic rule is that detuning the photon energy away from the resonance energy shortens the core-hole scatering duration time $\tau = 1/\sqrt{\Gamma^2 + \Omega^2}$, where Γ is the core-hole lifetime width and Ω is the detuning energy [102, 74]. This means that by detuning the photon energy over the resonance excitation we can manipulate the extent of geometry change before Auger decay, and thus having access to different region of PESs of final states.

A good starting point is to visualize to what extent the geometry changes following ammonia N1s-4a_1 excitation, studied in paper V. In ammonia switching from pyramidal geometry to planar geometry occurs within hydrogen motion on femtosecond timescale in competition with Auger decay. Considering angular distribution of H^+/NH_2^+ ion pair in the fixed in space molecule, where μ_z=$A_1 \otimes A_1 \otimes A_1$=$A_1$ [see Fig. 5.7 (a)], the initial alignment in the core-excited molecules with N-H bond angle of 53° with respect to the light polarization vector should lead to $\beta \rightarrow 1$, as shown by the black curve in Fig. 5.7 (a). This is, however, not the case if within the core-hole lifetime molecule evolves toward the planar geometry, as the bond angle changes with respect to the polarization vector of the light, leading $\beta \rightarrow 1$, as shown by the blue filled curve in Fig. 5.7 (b). The TIY spectrum of ammonia over the N1s-4a_1 and N1s-2e resonance excitations is shown in Fig. 5.7 (b). Geometry optimization calculation indicated an almost planar geometry as the equilibrium geometry of the N1s-4a_1 state, in which the potential barrier for the NH_2-H elongation has the highest value about 0.2 eV [see the schematic cuts of the PES thorough bending and stretching vibrational modes in Fig. 5.7 (c)]. Accordingly, as seen in Fig. 5.7 (d), angular distribution of the two-body H^+/NH_2^+ dissociation is dramatically changed

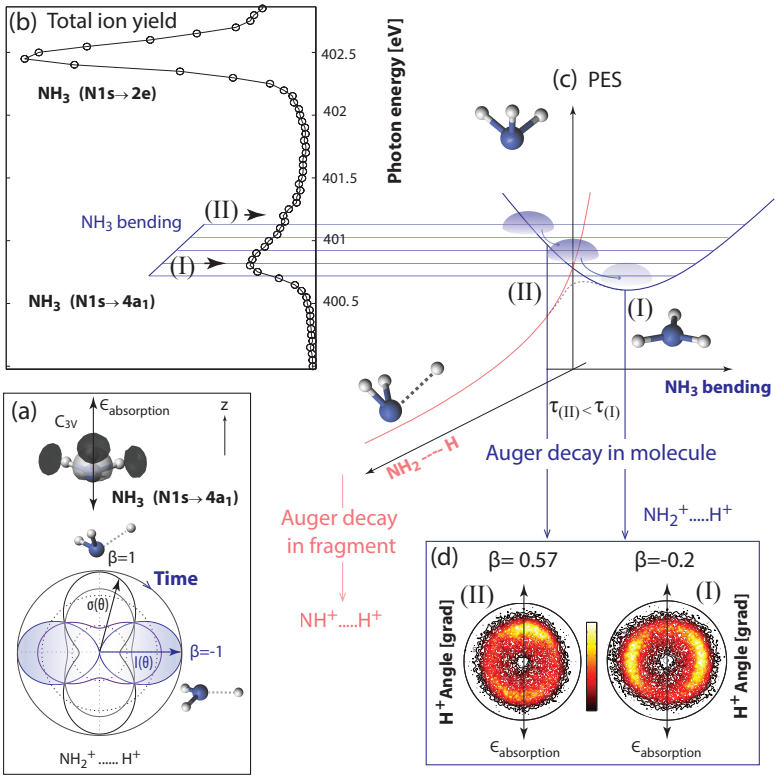

Figure 5.7: Molecular frame for NH_3 bending motion following N1s-4a_1 excitation(a). The angular distribution of H^+/NH_2^+ ion pair, I(θ), will indicate whether the core-hole lifetime works as a clock for evolution of nuclear geometry. Total ion yield of ammonia N1s excitation and associated vibrational features of N1s-4a_1 state (b). The schematic cuts of the PES of the N1-4a_1 state along NH_3 bending and N–H bond elongation coordinates (c). Histogram of angular distribution of H^+ detected in coincidence with NH_2^+ is presented for the resonance (I) and (II) excitations (d).

depending on the excitation to different regions of the PES of the core-excited state: while excitation to the low energy side of the PES (I) leads to β= -0.2 indicating long enough core-hole duration time for geometry change toward planar geometry, detuning the photon energy above the resonance (II) leads to β= 0.57 indicates that core-hole Auger decay occurs within the initial molecular geometry.

5.2.2 Site-selective C1s to π^* excitation in butadiene (Paper II)

One of the questions that is addressed in this thesis is whether site-selective localized core-electron excitation causes the molecules to preferentially dissociate around the site of excitation, and that to what extent nuclear geometry change prior to Auger

decay plays a role. A promising system for studying site-selective dissociation is butadiene. As discussed earlier, the extent of geometry change and "degree of localization" in Auger decay differs following terminal and central core electron excitation to the π^* orbital, which motivated us to look for site-selective dissociation in this molecule. The most straight forward way to visualize site-selective dissociation is using the partly deuteriated sample ($C_4H_2D_4$), in which terminal H is replaced with D. Considering three-body dissociation in the C_4D_6 sample where one D atom is ejected prior to charge separation into $C_2D_2^+/C_2D_3^+$ ion pair [see Fig. 4.7 (a)], in the $C_4H_2D_4$ sample this channel splits into two mass-separated $C_2HD^+/C_2HD_2^+$ and $C_2D_2^+/C_2HD_2^+$ channels, distinguishing terminal and central site of D/H ejection [see Fig. 4.7 (b)]. The yield of these channels as a function of photon energy [see Fig. 5.8 (a)] indicates that the rapid H/D ejection following core-electron excitation is a sensitive probe for "degree of hole localization" in Auger decay: whilst a terminal carbon core hole increases D ejection from the terminal site and decreases H ejection from the central site, a central core hole does not change the statistical pattern (measured on off-resonance excitation). It is not clear to us how fast H/D ejection after core-electron excitation is, but the dissociation yield shows while creation of a hole on the terminal site remains localized, creation of a hole on the central site dissipates completely. We can speculate that not only participator Auger decay of a terminal core hole is more localized than the central core hole, but also spectator Auger decay of terminal core hole to the double ionization continuum is more localized than the central core hole.

Regarding site-selective geometry change following core-hole localization the direction of the rapid H/D ejection is interesting to visualize. Considering angular correlation of the mass-distinguished fragments [see section 4.2.6] in planar butadiene, the out-of-plane symmetry breaking at the site of excitation (predicted by "Z+1" model) is reflected in the angle of H/D ejection, and consequently, is reflected on the histogram of the angles between two ionic fragments. The histogram of the angles between the ionic fragments in the three-body dissociation channels in C_4D_6 and $C_4H_2D_4$ samples are shown in Fig. 4.7 (c), (d), and (e). Following resonant excitation of the terminal carbon the angle between the ionic fragments extends to larger values compared to the excitation at higher photon energies. Considering constant KER of dissociation in these photon energies, the angular variation suggests that an out-of-plane geometry change occurs within the terminal core-hole lifetime, and mostly at the site of excitation. As predicted by the "Z+1" model different

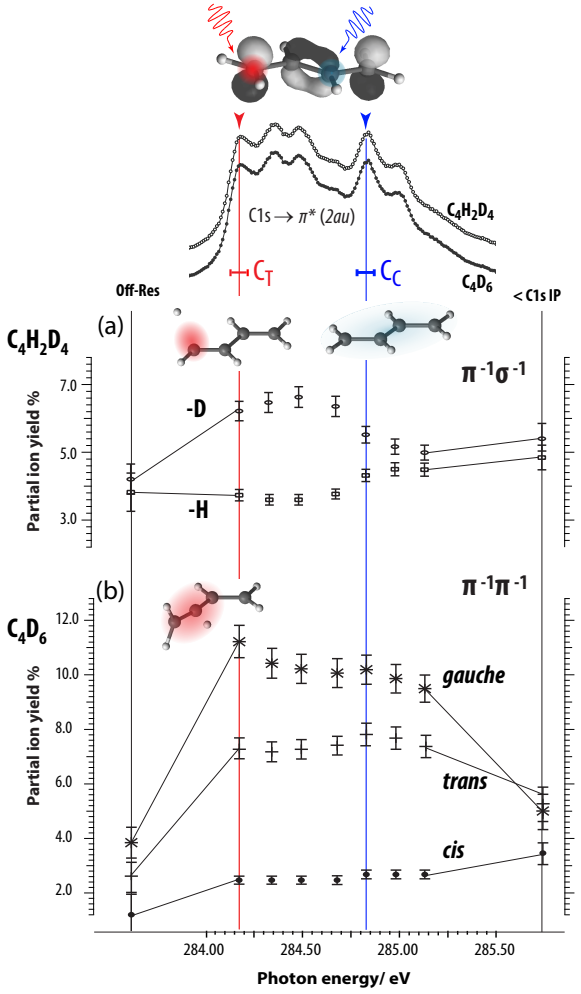

Figure 5.8: The role of site-selective terminal and central C1s-π^* excitation in butadiene is examined on the yields of dissociation channels corresponding to the rapid H/D ejection (a) and to the isomerization pathways (b).

behaviour following terminal and central C1s-π^* excitation is justified due to the different bonding character of the occupied π^* orbital on these sites (anti-bonding on terminal bonds and bonding on central bond).

Now we have examined our postulate (discussed in section 5.1.1) that site-selective out-of-plane motion in butadiene (or generally in π-conjugated system) determines the subsequent charge-transfer processes. If duration of the geometry change lasts long enough with respect to the core hole lifetime and during the Auger decay, final dissociation pathways are selectively launched. Ion yields corresponding to dissociation of different isomers are measured as a function of photon energy [Fig. 5.8 (b)]. As discussed in section 5.1.1, the *gauche* and *cis* pathways correspond to the gateway states in which dissociation is extensively launched toward out-of-plane symmetry breaking on terminal (CH_2 twisting) and central site (C-C torsion) respectively, and the *trans* pathway corresponds to the gateway state in which dissociation proceeds via direct symmetric charge separation. Accordingly, the longer the duration of out-of-plane geometry change in the core hole lifetime

and during the Auger decay, the more the *gauche* and *cis* pathways contribute to the dissociation. As seen in Fig. 5.8 (b) the *gauche* and *trans* dissociation pathways are enhanced upon C1s to π^* excitation, while the *cis* dissociation pathway is not affected. This is well justified due to longer timescale of heavy mass C-atom motion in *trans-cis* conformation compared to the shorter timescale of light mass H-atom motion in *trans-gauche* conformation. On the other hand, the extent of geometry change on the terminal core-hole lifetime is indicated on the relative ratio of *gauche* and *trans* pathways: while on resonant excitation of terminal C1s, where the extent of out-of-plane geometry change in the terminal core hole life time is the largest, the *gauche* pathway is more enhanced; while detuning the photon energy above the resonance, and also on resonance excitation of central C1s, the symmetric charge separation on the *trans* pathway increases. In summary, by comparison of dissociation following terminal and central core hole localization the mechanisms behind the site-selective dissociation are addressed: while extension of out-of-plane H-motion within the terminal core-hole lifetime increases site-selective dissociation (H-ejection and H-migration in *Gauche* dissociation), Auger decay of the planar geometry within the central core hole lifetime does not lead to localized dissociation.

5.2.3 C1s state-selective excitation in cyclopropane (Paper IV)

Another way to address the question of whether a core hole induced geometry change perturbs the many-body Auger effect is by comparing molecular dissociation for core-electron excitation to different valence orbitals. For this investigation, cyclopropane is an ideal example. In the triangular structure of carbon ring the degenerated C_{2p} orbitals are spatially distinguished in the x,y and z directions of molecule. As can be seen in the TIY spectrum of cyclopropane near the C1s edge shown in Fig. 5.9, C1s excitation to π^*_{ex} ($2a''_2$) and σ^*_{ex} ($1a'_2$) orbitals take place below the C1s ionization edge and C1s excitation to σ^*_{in} ($5e'$) orbitals is in the C1s continuum. Regarding different symmetry and anti-bonding characters over the ring-system on these orbitals ($2a''_2$ and $1a'_2$ are symmetric with respect to the molecular axis and $5e'$ is asymmetric), with selective excitation to these states different types of ring-deformations are induced.

In cyclopropane excitation of the equivalent C1s to symmetric orbitals gives rise to degenerate core-excited states, which in turn can couple vibronically through different modes of symmetry. Therefore, following C1s excitation to symmetric $2a''_2$ and $1a'_2$ orbitals evidence of ring-deformation coupling (Jahn-Teller distortion) is re-

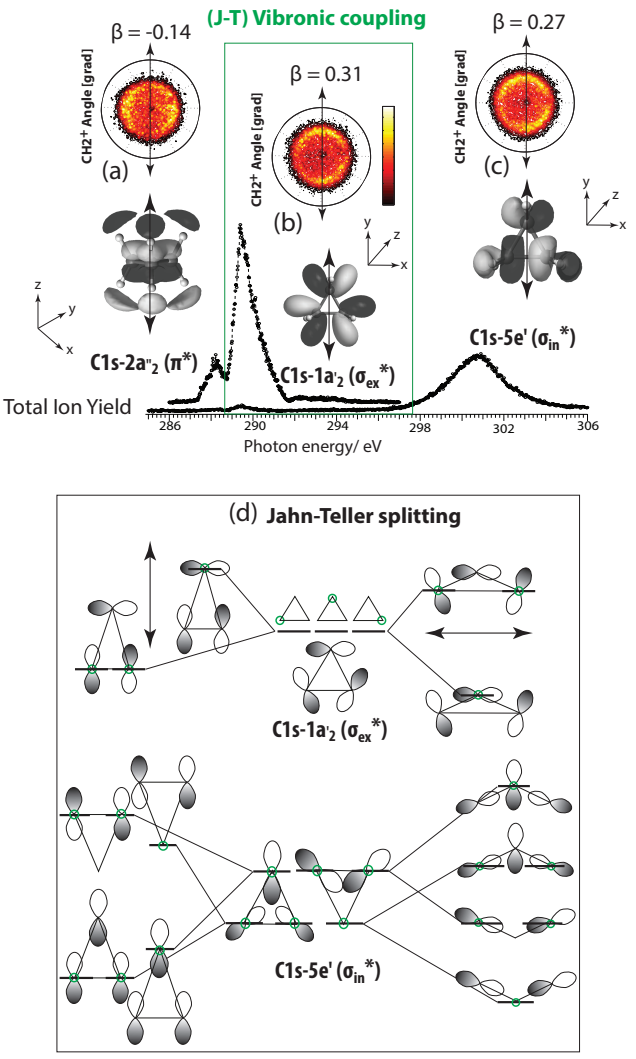

Figure 5.9: TIY spectrum for C1s to π^* and σ^* transitions in cyclopropane. The polar plots show angular anisotropy of CH_2^+ fragments recorded in coincidence with $C_2H_4^+$ fragments following C1s$\rightarrow$ $2a_2''$ (a), C1s$\rightarrow$ $1a_2'$ (b), and C1s$\rightarrow$ $5e'$ (c) excitations. The molecular alignment in C1s-$1a_2'$ transition created via Jahn-Teller (J-T) vibronic coupling of the degenerate states, and the Jahn-Teller distortion of degenerate states in C1s-$5e'$ transition (d).

flected in the angular distribution of fragments. In the polar plots (a)-(c) the angular distributions of the CH_2^+ ion recorded in coincidence with $C_2H_4^+$ for the three C1s resonance excitations are shown. While the corresponding β values for the C1s$\rightarrow$ $2a_2''$ (a) and C1s$\rightarrow$ $5e'$ (c) excitation are in qualitative agreement with the initial molecular alignment (see discussion in section 2.2.3); the anisotropic distribution with positive β value following C1s-$1a_2'$ excitation is evidence for Jahn-Teller active vibronic coupling in this transition. For C1s excitation to the symmetric $1a_2'$ orbital, as discussed in Section 2.2.3, no photo-absorption spatial-selectivity exists (see character Table. 2.1); however, an anisotropic distribution of the fragment with positive β value is recorded which indicates that the Jahn-Teller active ring-deformation vibrational mode e' is coupled to the transition. This means that following C1s-$1a_2'$ excitation the D_3h symmetry of equilateral triangle structure reduces toward two C_2v isosceles triangle minimum energy structures, by which a dipole moment is cre-

ated via one or two C-C bond elongation along the polarization vector of the light. Therefore, as seen in Fig. 5.9 (d), the three degenerate C1s states split into singly and doubly degenerate states where the potential energy of the core-excited states change depending on the location of the core-excited carbon with respect to the ring-deformation. It is worth mentioning that in the positive anisotropy of CH_2^+ angular distribution following C1s to 5e′ excitation the Jahn-Teller distortion can also be involved. Although in C1s-5e′ excitation the dipole matrix element is coordinated along x(y)-axes of the molecule, contribution of Jahn-Teller distortion leads to $\mu_{x(y)}$= ($A_1'\otimes$ E′ $\otimes$ E′) $\otimes$ E′ =A_1'+A_2'+3E′, and thus retains the initial molecular alignment. The Jahn-Teller splitting upon C1s-5e′ transition creates a complex situation due to the excitation of the three equivalent C1s to the doubly-degenerate 5e′ orbitals, in which a pair of three degenerate core-excited states splits into four states [see Fig. 5.9 (d)].

As discussed in Section 5.1.3, in cyclopropane the direction of ring-deformation dissociation is strongly connected to the symmetry of two charges/holes distribution over the ring-structure. Double ionization of doubly-degenerate 3e′ (σ-type) orbitals selectively determines the direction of ring-opening (C-C elongation): either two charges are symmetrically distributed over the ring (*uu/ud* states) leading to direct ring-opening into $CH_2^+/C_2H_4^+$ ion pair or two charges are asymmetrically distributed over the ring (*20/02* states) leading to Jahn-Teller distortion and creation of $C_3H_6^{2+}$ and $C_3H_4^{2+}$ isomers lying below the DIP_V, by which the molecule dissociates into $CH_3^+/C_2H_3^+$ and $H^+/C_2H_3^+$ ion pairs. In Fig. 5.10 the partial ion yield of dissociation following the C1s-$2a_2''(\pi^*)$, C1s-$1a_2'(\sigma_{ex}^*)$, and C1s-$5e'(\sigma_{in}^*)$ resonances are shown. The dissociation yields of the resonances are compared with off-resonance yields at 280 eV and above ionization at 320 eV. If the anti-bonding character of core-to-valence excitation remains long enough during the Auger decay, final dissociation pathways are selectively launched. If the anti-bonding character of π^* orbital on the CH_2 bonds (or bonding character on the C-C ring) remains at the Auger decay of C1s-π^* states, it will be reflected on the yield of C-H bond dissociation channels (or ring-closing pathways). If the anti-bonding character of σ^* orbitals on the C-C bonds remains during the Auger decay of C1s-σ^* states, it will be reflected on the yield of C-C bond dissociation. In panel (a) and (b) of Fig. 5.10, branching ratios of dissociation into $H_x^+/C_3H_y^+$ and $H^+/C_3H_y^+$ channels are seen to be enhanced by C1s-π^* excitation. An exception is the $H^+/C_3H_3^+$ channel which arises from ring-opening and is enhanced by C1s-σ_{in}^* excitation. In panel (c) of Fig. 5.10, branching

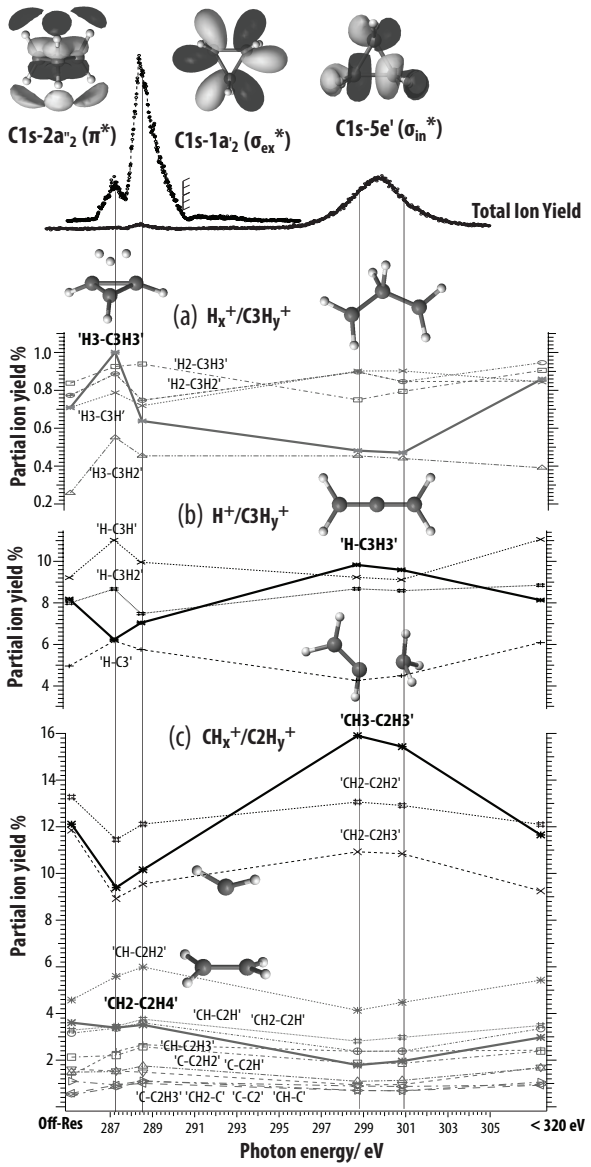

Figure 5.10: Partial ion yield of dissociation channels following cyclopropane C1s-2a$''_2(\pi^*)$, C1s-1a$'_2(\sigma^*_{ex})$, and C1s-5e$'(\sigma^*_{in})$ resonances.

ratios of dissociation into $CH_x^+/C_2H_y^+$ channels are seen to be enhanced upon C1s-σ^* resonance excitation, but behave differently upon C1s to σ^*_{ex} and σ^*_{in} excitation. The C1s excitation to the σ^*_{in} orbital, asymmetrically distributed anti-bonding character over the carbon ring, strongly enhances branching ratios of a few channels of high intensity, including $CH_3^+/C_2H_3^+$ ion pair representing Jahn-Teller distortion of the *20/02* dication states; while the C1s excitation to the σ^*_{ex} orbital, symmetrically distributed anti-bonding character over the carbon ring, to a lesser extent enhances these channels and slightly enhances variety of low intensity channels, including the $CH_2^+/C_2H_4^+$ ion pair representing the population of the repulsive *uu/ud* dication states. Considering the Jahn-Teller distortion in the C1s excitation to the σ^* orbitals, the relative ratios of $CH_3^+/C_2H_3^+$ and $CH_2^+/C_2H_4^+$ ion pairs indicates the extent of

Jahn-Teller distortion of these core-excited states. The lower relative ratio of 2.7 for the C1s-σ^*_{ex} excitation compared to the higher relative ratio of 8.9 for the C1s-σ^*_{in} excitation, thus, indicates a lower extent of Jahn-Teller distortion in the C1s-σ^*_{ex} compared to C1s-σ^*_{in} excitation.

5.3 Summary and Remarks

In this thesis, dissociation of two model systems were investigated: butadiene, a prototype of π-conjugated systems, and cyclopropane, prototype of the highly strained ring systems. The molecules absorb single photon and double ionize either via valence double ionization or after core-electron excitation via Auger decay. Dissociation dynamics within the double ionization continuum were investigated by means of a combined tunable light source with 3D-momenta coincident ion spectroscopy and with the help of *ab-initio* quantum calculation.

Dynamics of single photon double ionization in molecules are determined by dominant (electron-electron or electron-nucleus) correlation effects. In butadiene the photo absorption mainly occurs via direct (non-sequential) double ionization due to strongly correlated electrons contributing to the C-H and π bonds. This leads to dication species that are stabilized by the electron-exchange interaction, and dissociation pathways that are determined by hole/charge separation of the dication states. In cyclopropane with strongly correlated electron and nuclear motions photoabsorption mainly leads to indirect double ionization, via ring-deformation involving two electronic transitions. Consequently dissociation pathways are determined by nuclear dynamics on the intermediate states.

Nuclear dynamics within the femtosecond timescale of core-to-valence excited state determine the subsequent dynamics. We have found that the origin of site-selective dissociation in core-excited butadiene depends upon the different timescales for H atom and C atom motions. The sudden change in the nuclear charge of the terminal carbon in core-electron excitation induces H motion on the site of excitation. The H motion is initiated prior to Auger decay and enhances the contribution of H-migration pathways to the final states. However, the sudden change in the nuclear charge of the central carbon in core-electron excitation induces *trans-cis* motion which takes place on a longer timescale than the core-hole lifetime. Therefore, no site-selective effect is observed on the dissociation pattern. In cyclopropane excitation of equivalent C1s to σ^* orbitals leads to Jahn-Teller distortion of the ring-system

within the core-hole lifetime. The Jahn-Teller distortion lasts long enough so that dissociation pathways of the lower Jahn-Teller component in the double ionization continuum are enhanced.

The decisive moment in molecular photodissociation is on the femtosecond timescale when induced (charge migration + nuclear motion) many-body effects initiate molecular internal energy distribution. This means to obtain control over the molecular dissociation adequate knowledge about the underlying connection between electronic and nuclear motion is required. An advanced quantum calculation could of course be of great help in trying to understand the mechanism of isomerization reactions occurring on a few femtosecond timescale. However, one could also think of experiments with time-resolved multicoincidence photoelectron-photoion technique to collect more evidence regarding many-body correlation effects.

Bibliography

[1] P. Auger, "Sur l'effet photoélectrique composé," *J. Phys. Radium*, vol. 48, no. 6, pp. 205–208, 1925.

[2] V. Schmidt, "Photoionization of atoms using synchrotron radiation," *Reports on Progress in Physics*, vol. 55, no. 9, pp. 1483–1659, 1992.

[3] F. Yuichi and H. Sakai., *Electronic and Nuclear Dynamics in Molecular Systems*. World Scientific, 2011.

[4] J. R. Lakowicz, ed., *Principles of Fluorescence Spectroscopy*. Springer Nature, 2006.

[5] X. Zhang, X. Li, D. Zhang, N. Q. Su, W. Yang, H. O. Everitt, and J. Liu, "Product selectivity in plasmonic photocatalysis for carbon dioxide hydrogenation," *Nature Communications*, vol. 8, p. 14542, feb 2017.

[6] X. Hu, Z. Qureishi, and S. W. Thomas, "Light-controlled selective disruption, multilevel patterning, and sequential release with polyelectrolyte multilayer films incorporating four photocleavable chromophores," *Chemistry of Materials*, mar 2017.

[7] K. Pande, C. D. M. Hutchison, G. Groenhof, A. Aquila, J. S. Robinson, J. Tenboer, S. Basu, S. Boutet, D. P. DePonte, M. Liang, T. A. White, N. A. Zatsepin, O. Yefanov, D. Morozov, D. Oberthuer, C. Gati, G. Subramanian, D. James, Y. Zhao, J. Koralek, J. Brayshaw, C. Kupitz, C. Conrad, S. Roy-Chowdhury, J. D. Coe, M. Metz, P. L. Xavier, T. D. Grant, J. E. Koglin, G. Ketawala, R. Fromme, V. rajer, R. Henning, J. C. H. Spence, A. Ourmazd, P. Schwander, U. Weierstall, M. Frank, P. Fromme, A. Barty, H. N. Chapman, K. Moffat, J. J. van Thor, and M. Schmidt, "Femtosecond structural dynamics drives the trans/cis isomerization in photoactive yellow protein," *Science*, vol. 352, pp. 725–729, may 2016.

[8] W. Eberhardt, T. K. Sham, R. Carr, S. Krummacher, M. Strongin, S. L. Weng, and D. Wesner, "Site-specific fragmentation of small molecules following soft-x-ray excitation," *Phys. Rev. Lett.*, vol. 50, no. 14, pp. 1038–1041, 1983.

[9] C. E. Liekhus-Schmaltz, I. Tenney, T. Osipov, A. Sanchez-Gonzalez, N. Berrah, R. Boll, C. Bomme, C. Bostedt, J. D. Bozek, S. Carron, R. Coffee, J. Devin, B. Erk, K. R. Ferguson, R. W. Field, L. Foucar, L. J. Frasinski, J. M. Glownia, M. Gühr, A. Kamalov, J. Krzywinski, H. Li, J. P. Marangos, T. J. Martinez, B. K. McFarland, S. Miyabe, B. Murphy, A. Natan, D. Rolles, A. Rudenko, M. Siano, E. R. Simpson, L. Spector, M. Swiggers, D. Walke, S. Wang, T. Weber, P. H. Bucksbaum, and V. S. Petrovic, "Ultrafast isomerization initiated by x-ray core ionization," *Nature Communications*, vol. 6, p. 8199, 2015.

[10] C. Miron, M. Simon, N. Leclercq, D. L. Hansen, and P. Morin, "Site-selective photochemistry of core excited molecules: Role of the internal energy," *Physical Review Letters*, vol. 81, no. 19, pp. 4104–4107, 1998.

[11] R. Weinkauf, P. Aicher, G. Wesley, J. Grotemeyer, and E. W. Schlag, "Femtosecond versus nanosecond multiphoton ionization and dissociation of large molecules," *The Journal of Physical Chemistry*, vol. 98, no. 34, pp. 8381–8391, 1994.

[12] R. Weinkauf, P. Schanen, A. Metsala, E. W. Schlag, M. Bürgle, and H. Kessler, "Highly efficient charge transfer in peptide cations in the gas phase: threshold effects and mechanism," *The Journal of Physical Chemistry*, vol. 100, no. 47, pp. 18567–18585, 1996.

[13] P. E. Nielsen, ed., *Photochemical Probes in Biochemistry.* Springer Nature, 1989.

[14] K. P. Lu, G. Finn, T. H. Lee, and L. K. Nicholson, "Prolyl cis-trans isomerization as a molecular timer," *Nature Chemical Biology*, vol. 3, pp. 619–629, oct 2007.

[15] T. Kobayashi, T. Saito, and H. Ohtani, "Real-time spectroscopy of transition states in bacteriorhodopsin during retinal isomerization," *Nature*, vol. 414, pp. 531–534, nov 2001.

[16] O. Björneholm, S. Sundin, S. Svensson, R. R. T. Marinho, A. Naves de Brito, F. Gel'mukhanov, and H. Ågren, "Femtosecond dissociation of core-excited hcl monitored by frequency detuning," *Phys. Rev. Lett.*, vol. 79, pp. 3150–3153, 1997.

[17] I. Hjelte, M. Piancastelli, R. Fink, O. Björneholm, M. Bässler, R. Feifel, A. Giertz, H. Wang, K. Wiesner, A. Ausmees, C. Miron, S. Sorensen, and S. Svensson, "Evidence for ultra-fast dissociation of molecular water from resonant auger spectroscopy," *Chemical Physics Letters*, vol. 334, pp. 151–158, feb 2001.

[18] H. Hertz, "Ueber einen einfluss des ultravioletten lichtes auf die electrische entladung," *Annalen der Physik und Chemie*, vol. 267, no. 8, pp. 983–1000, 1887.

[19] A. Einstein, "Über einen die Erzeugung und Verwandlung des Lichtes betreffenden heuristischen Gesichtspunkt," *Annalen der Physik*, vol. 17, pp. 132–148, 1905. Translated by D. ter Haar: On a Heuristic Point of View about the Creation and Conversion of Light. In *The Old Quantum Theory*, 91–107 (http://users.physik.fu-berlin.de/ kleinert/files/eins$_l q.pdf Pergamon Press$, 1967).

[20] T. Koopmans, "Über die zuordnung von wellenfunktionen und eigenwerten zu den einzelnen elektronen eines atoms," *Physica*, vol. 1, no. 1-6, pp. 104–113, 1934.

[21] R. S. Mulliken, "Spectroscopy, molecular orbitals, and chemical bonding," *Science*, vol. 157, no. 3784, pp. 13–24, 1967.

[22] R. K. Harris, E. D. Becker, S. M. C. de Menezes, R. Goodfellow, and P. Granger, "NMR nomenclature. nuclear spin properties and conventions for chemical shifts(IUPAC recommendations 2001)," *Pure and Applied Chemistry*, vol. 73, no. 11, 2001.

[23] L. S. Cederbaum, W. Domcke, J. Schirmer, W. von Niessen, G. H. F. Diercksen, and W. P. Kraemer, "Correlation effects in the ionization of hydrocarbons," *The Journal of Chemical Physics*, vol. 69, no. 4, p. 1591, 1978.

[24] L. S. Cederbaum and J. Zobeley *Chem. Phys. Lett.*, vol. 307, p. 205, 1999.

[25] J. Breidbach and L. S. Cederbaum *J. Chem. Phys.*, vol. 118, p. 3983, 2003.

[26] F. Calegari, D. Ayuso, A. Trabattoni, L. Belshaw, S. D. Camillis, S. Anumula, F. Frassetto, L. Poletto, A. Palacios, P. Decleva, J. B. Greenwood, F. Martin, and M. Nisoli, "Ultrafast electron dynamics in phenylalanine initiated by attosecond pulses," *Science*, vol. 346, no. 6207, pp. 336–339, 2014.

[27] T. A. Carlson, "Double electron ejection resulting from photo-ionization in the outermost shell of he, ne, and ar, and its relationship to electron correlation," *Physical Review*, vol. 156, no. 1, pp. 142–149, 1967.

[28] J. Als-Nielsen and D. McMorrow, *Elements of Modern X-ray Physics*. Wiley-Blackwell, 2011.

[29] L. Meitner, "Über die entstehung der -strahl-spektren radioaktiver substanzen," *Zeitschrift für Physik*, vol. 9, pp. 131–144, 1922.

[30] M. Coville and T. D. Thomas *Phys. Rev. Lett. A.*, vol. 43, p. 11, 1991.

[31] J. N. Cutler, G. M. Bancroft, D. G. Sutherland, and K. H. Tan, "Chemical dependence of core-level linewidths and ligand-field splittings: High-resolution core-level photoelectron spectra of iodine 4d levels," *Physical Review Letters*, vol. 67, no. 12, pp. 1531–1534, 1991.

[32] M. Coville and T. D. Thomas, "Molecular effects on inner-shell lifetimes: Possible test of the one-center model of auger decay," *Physical Review A*, vol. 43, no. 11, pp. 6053–6056, 1991.

[33] H. Aksela, S. Aksela, H. Pulkkinen, A. Kivimäki, and O.-P. Sairanen, "Shake processes in auger decay of resonantly excited states of rare gases," *Physica Scripta*, vol. 41, no. 4, pp. 425–428, 1990.

[34] M. Born and R. Oppenheimer, "Zur quantentheorie der molekeln," *Annalen der Physik*, vol. 389, no. 20, pp. 457–484, 1927.

[35] F. X. Gadea, H. Köppel, J. Schirmer, L. S. Cederbaum, K. J. Randall, A. M. Bradshaw, Y. Ma, F. Sette, and C. T. Chen *Phys. Rev. Lett.*, vol. 66, p. 883, 1991.

[36] Y. Ma, F. Sette, G. Meigs, S. Modesti, and C. T. Chen, "Breaking of ground-state symmetry in core-excited ethylene and benzene," *Physical Review Letters*, vol. 63, no. 19, pp. 2044–2047, 1989.

[37] D. Holland, L. Karlsson, and K. Siegbahn, "A reinvestigation of the vibrational structure and the orbital assignments in the photoelectron bands of cyclopropane," *Journal of Electron Spectroscopy and Related Phenomena*, vol. 125, no. 1, pp. 57–68, 2002.

[38] H. A. Jahn and E. Teller, "Stability of polyatomic molecules in degenerate electronic states. i. orbital degeneracy," *Proceedings of the Royal Society A: Mathematical, Physical and Engineering Sciences*, vol. 161, no. 905, pp. 220–235, 1937.

[39] E. Haselbach, "Jahn-teller distortions in the radical cations of cyclopropane and allene," *Chemical Physics Letters*, vol. 7, no. 4, pp. 428–430, 1970.

[40] F. X. Gadea, S. Mathieu, and L. S. Cederbaum *J. Mol. Struct. (Theochem)*, vol. 401, p. 15, 1997.

[41] B.-K. Teo and P. A. Lee, "Ab initio calculations of amplitude and phase functions for extended x-ray absorption fine structure spectroscopy," *Journal of the American Chemical Society*, vol. 101, no. 11, pp. 2815–2832, 1979.

[42] N. V. Kryzhevoi, N. V. Dobrodey, and L. S. Cederbaum, "Core-hole hamiltonians and corrected equivalent core model for systems with equivalent atoms," *The Journal of Chemical Physics*, vol. 119, no. 23, pp. 12138–12152, 2003.

[43] K. Yamanouchi, D. Charalambidis, and D. Normand, eds., *Progress in Ultrafast Intense Laser Science VII*. Springer Berlin Heidelberg, 2011.

[44] P. A. M. Dirac, *The Quantum Theory of the Emission and Absorption of Radiation*, vol. 114. The Royal Society, 1927.

[45] R. N. Zare, "Photoejection dynamics," *Mol. Photochem.*, vol. 4, pp. 1–37, 1972.

[46] S.-c. Yang and R. Bersohn, "Theory of the angular distribution of molecular photofragments," *J. Chem. Phys.*, vol. 61, no. 11, pp. 4400–4407, 1974.

[47] L. P. Kadanoff, *More is the Same Phase Transitions and Mean Field Theories*, vol. 137. Springer Nature, 2009.

[48] D. R. Hartree, *The Wave Mechanics of an Atom with a Non-Coulomb Central Field. Part I. Theory and Methods*, vol. 24. Cambridge University Press (CUP), 1928.

[49] S. H. Ashworth, *Molecular Quantum Mechanics, 5th edn, by Peter Atkins and Ronald Friedman*, vol. 53. Informa UK Limited, 2012.

[50] R. Ditchfield, W. J. Hehre, and J. A. Pople, "Self-consistent molecular-orbital methods. IX. an extended Gaussian-type basis for molecular-orbital studies of organic molecules," *The Journal of Chemical Physics*, vol. 54, no. 2, pp. 724–728, 1971.

[51] T. H. Dunning, "Gaussian basis sets for use in correlated molecular calculations. i. the atoms boron through neon and hydrogen," *The Journal of Chemical Physics*, vol. 90, no. 2, pp. 1007–1023, 1989.

[52] T. Sommerfeld, "Lorentz trial function for the hydrogen atom: A simple, elegant exercise," *Journal of Chemical Education*, vol. 88, no. 11, pp. 1521–1524, 2011.

[53] T. S. Carlton, "Correlated wavefunctions for the ground state of H-, He, and Li," *The Journal of Chemical Physics*, vol. 53, no. 11, pp. 4234–4237, 1970.

[54] P.-O. Löwdin, "Quantum theory of many-particle systems. i. physical interpretations by means of density matrices, natural spin-orbitals, and convergence problems in the method of configurational interaction," *Physical Review*, vol. 97, no. 6, pp. 1474–1489, 1955.

[55] B. O. Roos, P. R. Taylor, and P. E. Sigbahn, "A complete active space SCF method (CASSCF) using a density matrix formulated super-CI approach," *Chemical Physics*, vol. 48, no. 2, pp. 157–173, 1980.

[56] D. Ma, G. L. Manni, and L. Gagliardi, "The generalized active space concept in multiconfigurational self-consistent field methods," *The Journal of Chemical Physics*, vol. 135, no. 4, p. 044128, 2011.

[57] S. Vancoillie, M. G. Delcey, R. Lindh, V. Vysotskiy, P.-Å. Malmqvist, and V. Veryazov, "Parallelization of a multiconfigurational perturbation theory," *J. Comput. Chem.*, vol. 34, no. 22, pp. 1937–1948, 2013.

[58] P. A. Malmqvist, A. Rendell, and B. O. Roos, "The restricted active space self-consistent-field method, implemented with a split graph unitary group approach," *The Journal of Physical Chemistry*, vol. 94, no. 14, pp. 5477–5482, 1990.

[59] V. Veryazov, P. Å. Malmqvist, and B. O. Roos, "How to select active space for multiconfigurational quantum chemistry," *International Journal of Quantum Chemistry*, vol. 111, no. 13, pp. 3329–3338, 2011.

[60] F. Aquilante, J. Autschbach, R. K. Carlson, L. F. Chibotaru, M. G. Delcey, L. D. Vico, I. F. Galván, N. Ferré, L. M. Frutos, L. Gagliardi, M. Garavelli, A. Giussani, C. E. Hoyer, G. L. Manni, H. Lischka, D. Ma, P. Å. Malmqvist, T. Müller, A. Nenov, M. Olivucci, T. B. Pedersen, D. Peng, F. Plasser, B. Pritchard, M. Reiher, I. Rivalta, I. Schapiro, J. Segarra-Martí, M. Stenrup, D. G. Truhlar, L. Ungur, A. Valentini, S. Vancoillie, V. Veryazov, V. P. Vysotskiy, O. Weingart, F. Zapata, and R. Lindh, *Molcas8: New capabilities for multiconfigurational quantum chemical calculations across the periodic table*, vol. 37. Wiley-Blackwell, 2015.

[61] W. C. Davidon, "Variable metric method for minimization," *SIAM Journal on Optimization*, vol. 1, no. 1, pp. 1–17, 1991.

[62] P. Hohenberg and W. Kohn, "Inhomogeneous electron gas," *Physical Review*, vol. 136, no. 3B, pp. B864–B871, 1964.

[63] W. Kohn and L. J. Sham, "Self-consistent equations including exchange and correlation effects," *Physical Review*, vol. 140, no. 4A, pp. A1133–A1138, 1965.

[64] L. Antonov, ed., *Tautomerism*. Wiley-Blackwell, 2016.

[65] Å. Andersson, M. Eriksson, L.-J. Lindgren, Röjsel, P., and S. Werin, "The new 1.5 GeV storage ring for synchrotron radiation: MAX II," *Rev. Sci. Instrum.*, vol. 66, no. 2, pp. 1850–1853, 1995.

[66] T. Balasubramanian, B. N. Jensen, S. Urpelainen, B. Sommarin, U. Johansson, M. Huttula, R. Sankari, E. Nommiste, S. Aksela, H. Aksela, R. Nyholm, R. Garrett, I. Gentle, K. Nugent, and S. Wilkins, "The normal incidence monochromator beamline i3 on MAX III," 2010.

[67] S. Urpelainen, M. Huttula, T. Balasubramanian, R. Sankari, P. Kovala, E. Kukk, E. N. ommiste, S. Aksela, R. Nyholm, H. Aksela, R. Garrett, I. Gentle, K. Nugent, and S. Wilkins, "FINEST: a high performance branch-line for VUV photon energy range gas phase studies at MAX-lab," 2010.

[68] M. Bässler, J.-O. Forsell, O. Björneholm, R. Feifel, M. Jurvansuu, S. Aksela, S. Sundin, S. Sorensen, R. Nyholm, A. Ausmees, and S. Svensson, "Soft x-ray undulator beam line I411 at MAX-II for gases, liquids and solid samples," *Journal of Electron Spectroscopy and Related Phenomena*, vol. 101-103, pp. 953–957, 1999.

[69] J. Larmor, *A Dynamical Theory of the Electric and Luminiferous Medium. Part III. Relations with Material Media*, vol. 190. The Royal Society, 1897.

[70] S. Mobilio, F. Boscherini, and C. Meneghini, eds., *Synchrotron Radiation*. Springer Nature, 2015.

[71] I. H. Suzuki, A. Nitta, H. Fukuzawa, K. Ueda, O. Takahashi, Y. Tamenori, and S. Nagaoka, "Site-specific behavior in de-excitation spectra of F3SiCH2CH2Si(CH3)3 in the Si 1s excitation region," *The Journal of Chemical Physics*, vol. 131, no. 16, p. 164309, 2009.

[72] J. Eland, P. Linusson, M. Mucke, and R. Feifel, "Homonuclear site-specific photochemistry by an ion–electron multi-coincidence spectroscopy technique," *Chemical Physics Letters*, vol. 548, pp. 90 – 94, 2012.

[73] O. Björneholm, S. Sundin, S. Svensson, R. R. T. Marinho, A. N. de Brito, F. Gel'mukhanov, and H. Ågren, "Femtosecond dissociation of core-excited HCl monitored by frequency detuning," *Physical Review Letters*, vol. 79, no. 17, pp. 3150–3153, 1997.

[74] M. N. Piancastelli, "Auger resonant raman studies of atoms and molecules," *Journal of Electron Spectroscopy and Related Phenomena*, vol. 107, no. 1, pp. 1–26, 2000.

[75] J. Laksman, D. Céolin, E. P. Månsson, S. L. Sorensen, and M. Gisselbrecht, "Development and characterization of a multiple-coincidence ion-momentum imaging spectrometer," *Rev. Sci. Instrum.*, vol. 84, no. 12, p. 123113, 2013.

[76] A. Lindgren, *Studies of Molecular and Cluster Fragmentation Using Synchrotron Radiation: Measurements and Models*. Ph.D thesis, Lund University, 2006.

[77] W. C. Wiley and I. H. McLaren, "Time-of-flight mass spectrometer with improved resolution," *Rev. Sci. Instrum.*, vol. 26, no. 12, pp. 1150–1157, 1955.

[78] RoentDek Handels GmbH, "http://www.roentdek.de/manuals/."

[79] A. Adams and F. H. Read, "Electrostatic cylinder lenses III: three element asymmetric voltage lenses," *J. Phys. E: Sci. Instrum.*, vol. 5, no. 2, p. 156, 1972.

[80] W. Eberhardt, E. Plummer, I. W. Lyo, R. Reininger, R. Carr, W. Ford, and D. Sondericker, "Auger electron-ion coincidence studies to determine the pathways in soft x-ray induced fragmentation of isolated molecules," *Australian Journal of Physics*, vol. 39, no. 5, p. 633, 1986.

[81] A. S. Newton and A. F. Sciamanna, "Metastable dissociation of the doubly charged carbon monoxide ion," *The Journal of Chemical Physics*, vol. 53, no. 1, pp. 132–136, 1970.

[82] C. P. Safvan and D. Mathur, "On the determination of the lifetime of metastable doubly charged molecules by ion translational energy spectrometry: CO2," *Journal of Physics B: Atomic, Molecular and Optical Physics*, vol. 26, no. 22, pp. L793–L798, 1993.

[83] A. E. Slattery, T. A. Field, M. Ahmad, R. I. Hall, J. Lambourne, F. Penent, P. Lablanquie, and J. H. D. Eland, "Spectroscopy and metastability of CO2 molecular dicatios," *The Journal of Chemical Physics*, vol. 122, no. 8, p. 084317, 2005.

[84] J. Laksman, *Nuclear motion in molecular ions studied with synchrotron radiation and multicoincidence momentum imaging spectrometry.* Ph.D thesis, Lund University, 2012.

[85] R. Locht and J. Momigny, "The double ionization of ammonia. its dissociation into the doubly ionized fragment N2," *Chemical Physics Letters*, vol. 138, no. 5, pp. 391–396, 1987.

[86] R. H. Dalitz, "Decay of mesons of known charge," *Physical Review*, vol. 94, no. 4, pp. 1046–1051, 1954.

[87] K. Ueda and J. H. D. Eland, "Molecular photodissociation studied by VUV and soft x-ray radiation," *Journal of Physics B: Atomic, Molecular and Optical Physics*, vol. 38, no. 9, pp. S839–S859, 2005.

[88] I. Hjelte, M. Piancastelli, C. Jansson, K. Wiesner, O. Björneholm, M. Bässler, S. Sorensen, and S. Svensson, "Evidence of ultra-fast dissociation in ammonia observed by resonant Auger electron spectroscopy," *Chemical Physics Letters*, vol. 370, no. 5-6, pp. 781–788, 2003.

[89] A. Rouzée, P. Johnsson, L. Rading, A. Hundertmark, W. Siu, Y. Huismans, S. Düsterer, H. Redlin, F. Tavella, N. Stojanovic, A. Al-Shemmary, F. Lépine, D. M. P. Holland, T. Schlatholter, R. Hoekstra, H. Fukuzawa, K. Ueda, and M. J. J. Vrakking, "Towards imaging of ultrafast molecular dynamics using FELs," *J. Phys. B: At., Mol. Opt. Phys.*, vol. 46, no. 16, p. 164029, 2013.

[90] Y. Jiang, A. Senftleben, A. Rudenko, M. E. Madjet, O.Vendrell, M. Kurka, K. Schnorr, L. Foucar, M. Kübel, O. Herrwerth, M. Lezius, M. Kling, J. van Tilborg, A. Belkacem, K. Ueda, S. Düsterer, R. Treusch, C. Schröter, R. Santra, J. Ullrich, and R. Moshammer, "Watching the acetylene vinylidene intramolecular reaction in real time," *Preprint*, 2014.

[91] R. Thissen, J. Delwiche, J. M. Robbe, D. Duflot, J. P. Flament, and J. H. D. Eland, "Dissociations of the ethyne dication C2H2," *The Journal of Chemical Physics*, vol. 99, no. 9, pp. 6590–6599, 1993.

[92] X. Gong, Q. Song, Q. Ji, H. Pan, J. Ding, J. Wu, and H. Zeng, "Strong-field dissociative double ionization of acetylene," *Physical Review Letters*, vol. 112, no. 24, 2014.

[93] M. Alagia, P. Candori, S. Falcinelli, F. Pirani, M. S. P. Mundim, R. Richter, M. Rosi, S. Stranges, and F. Vecchiocattivi, "Dissociative double photoionization of benzene molecules in the 26–33 eV energy range," *Physical Chemistry Chemical Physics*, vol. 13, no. 18, p. 8245, 2011.

[94] E. Bergmann, "Isomerization of unsaturated hydrocarbons.," *Chemical Reviews*, vol. 29, no. 3, pp. 529–551, 1941.

[95] A. S. Alnaser, I. Litvinyuk, T. Osipov, B. Ulrich, A. Landers, E. Wells, C. M. Maharjan, P. Ranitovic, I. Bochareva, D. Ray, and C. L. Cocke, "Momentum-imaging investigations of the dissociation and the isomerization of acetylene to vinylidene by intense short laser pulses," *Journal of Physics B: Atomic, Molecular and Optical Physics*, vol. 39, no. 13, p. S485, 2006.

[96] M. Kübel, R. Siemering, C. Burger, N. G. Kling, H. Li, A. Alnaser, B. Bergues, S. Zherebtsov, A. Azzeer, I. Ben-Itzhak, R. Moshammer, R. de Vivie-Riedle, and M. Kling, "Steering proton migration in hydrocarbons using intense few-cycle laser fields," *Physical Review Letters*, vol. 116, no. 19, 2016.

[97] T. Masuoka, I. Koyano, and N. Saito, "Anisotropic angular distribution of fragment ions in dissociative double photoionization of OCS," *Physical Review A*, vol. 44, no. 7, pp. 4309–4315, 1991.

[98] T. Masuoka, "Observation of anisotropic angular distribution of ionic fragments in the dissociation of CO2," *Physical Review A*, vol. 50, no. 3, pp. 2298–2303, 1994.

[99] G. C. King, D. B. Thompson, G. Dawber, and N. Gulley, "Photo-double ionization and the role of indirect processes in molecules," vol. 392, p. 185, 1997.

[100] J. H. D. Eland, P. Lablanquie, M. Lavollée, M. Simon, R. I. Hall, M. Hochlaf, and F. Penent, "Double photoionization of IMG below the double ionization potential," *Journal of Physics B: Atomic, Molecular and Optical Physics*, vol. 30, no. 9, p. 2177, 1997.

[101] R. Feifel, J. H. D. Eland, and D. Edvardsson, "Valence double ionization of O2 at photon energies below and above the molecular double ionization threshold," *The Journal of Chemical Physics*, vol. 122, no. 14, p. 144308, 2005.

[102] P. Skytt, P. Glans, J.-H. Guo, K. Gunnelin, C. Såthe, J. Nordgren, F. K. Gel'mukhanov, A. Cesar, and H. Ågren, "Quenching of symmetry breaking in resonant inelastic x-ray scattering by detuned excitation," *Physical Review Letters*, vol. 77, no. 25, pp. 5035–5038, 1996.

Acknowledgments

First of all, I would like to thank my supervisor, Prof. Stacey Sorensen, for all of your support, enthusiasm, inspiration, and immense knowledge. It was a great luck to have you as a supervisor who cared so much about my work, and who is responded to my questions so patiently and friendly. It was not only science and scientific language that you have taught me, but also I learned from you how to positively think and behave in different situations.

Secondly, I thank Dr. Mathieu Gisselbrtecht for being my co-supervisor, and several discussions during this thesis work, and for often doing the difficult work during the beamtimes, which could not be as fun and fruitful in your absence. I would also like to thank the rest of the group for assisting me in many different ways. Dr. Anna Sankari, Dr. Noelle Walsh, Dr. Erik Mansson, Dr. Joakim Laksman, Bart Oostenrijk, and Christian Stråhlman, deserve special mention for making a friendly and engaging atmosphere to work. I thank Dr. Noelle Walsh for sharing your experiences in experimental physics, I thank Dr. Anna Sankari for sharing your experiences in quantum calculation, and I also thank Dr. Erik Mansson and Dr. Joakim Laksman for leaving your valuable Ph.D theses. I would also like to thank Dr. Maxim Tchaplyguine for your patient, help, and company during the beamtimes. The help of the other staff of Max lab during the beamtimes is also acknowledged.

I sincerely thank all former and present members of the Division of Synchrotron Radiation Research for their discussions and amiable surroundings. Prof. Joachim Schnadt is greatly acknowledged for leading the very useful journal club meetings, and together with Patrik Wirgin are acknowledged for taking care of all the non-scientific papers related work.

I thank Dr. Gunnar Ohrwall for reviewing my thesis and for constructive comments. I would also thank Prof. Marc Simon who is going to be the faculty opponent and Prof. Jesper Andersen who is going to chair the dissertation. The financial support from the Knut and Alice Wallenberg foundation and the Swedish Research

Council (VR) are also acknowledged.

Finally I would like to thank my family members and friends for theirs affection and patience. I thank my parents and sisters (Shaghayegh and Mehrnoush) for assisting me in different ways. I specially thank my friend Rabs for standing by me all the time with supporting and encouraging.